京都大学　防災研究所
Disaster Prevention Research Institute
Kyoto University

International Collaborative Research
2023IG-03

# Experimental Investigations on Particle Behavior in Stormwater Tanks for Numerical Simulation

令和 6 年 5 月

May，2024

研究代表者
Coordinator

Christian Auel

# Summary

Pumped storage power plants have become increasingly important in recent years due to the progression of the energy transition and the expansion of renewable energy production. A key advantage of pumped storage power plants is the ability to store electrical energy with a high degree of efficiency. However, increasing sedimentation can be observed in reservoirs worldwide, including the upper basins of pumped storage power plants, which can have a negative impact on various aspects of these power plants, including efficiency and stability.

This study is part of a larger project addressing the issue of sedimentation in the upper basin of pumped storage power plants with the aim of better understanding the mechanisms and formulating solutions. In this study, the flow patterns in a model basin representing an upper basin of a pumped storage power plant are investigated. The main objective is to gain basic knowledge and data about the structure of this flow in order to be able to create numerical simulations based on it. The main aim of the project is to prevent the sedimentation in the upper basins of pumped storage power plants.

In this context, the basics of pumped storage power plants and the problem of sedimentation were explained, the recording of flow patterns using Particle Image Velocimetry (PIV) was discussed and the design and implementation of model tests were explained. Subsequently, several possible model basins were designed, of which the prototypes do not exist in reality, but are based on the dimensions of real upper basins of pumped storage power plants. The test setup with the constructed model basin was then optimized in order to make the best possible use of the recordings for a PIV evaluation. In the next step, the recorded videos were evaluated using the Fudaa-LSPIV software and the generated flow patterns were presented and discussed. Finally, possible solutions to prevent the sedimentation in upper basins of pumped storage plants power were suggested.

# Table of Contents

# List of Figures

# List of Tables

# List of Abbreviations

| Abbreviation | Description |
|---|---|
| A | Surface area |
| $d_h$ | Hydraulic diameter |
| FPS | Frames per Second |
| Fr | Froude number |
| h | Height |
| IA | Interrogation Area |
| LSPIV | Large Scale Particle Image Velocimetry |
| LSV | Laser Speckle Velocimetry |
| $L_{tot.}$ | Total length |
| M | Scale |
| MID | Magnetic-inductive flow meter |
| PIV | Particle Image Velocimetry |
| PTV | Particle Tracking Velocimetry |
| Re | Reynolds number |
| SA | Searching Area |
| t | Time |
| v | Velocity |
| $\nu$ | Kinematic viscosity |

# 1 Introduction

## 1.1 Lead-in

The energy transition has significantly increased the share of renewable energy in electricity consumption in Germany. In 2022, this share amounted to 46.2% of gross electricity consumption and is set to rise to at least 80% by 2030. Most of this energy is generated from wind and solar power plants, although these are volatile depending on the weather situation. In addition, electricity consumption fluctuates greatly throughout the day and year. (cf. Bundesregierung 2023)

Caloric power plants, such as nuclear power plants or coal-fired power plants, can only adapt their energy production to fluctuating energy demand to a limited extent or not at all. It is therefore already important and will be even more important in the future to store energy at times of low consumption (at night) or high production (favorable weather conditions). Pumped storage power plants are to this day the only way to store electrical energy with an acceptable level of efficiency and make it available again within a very short time. Due to these properties, pumped storage plants are important structures for providing peak energy and maintaining the frequency of the electricity grid. (cf. Mohringer 2022)

However, the artificial storage basins interrupt the continuity of sediment transport in the natural watercourse where the basin was built. Due to the low flow velocities in the basins, the transported sediments settle and reduce the storage volume. These volume losses impair the reliability, efficiency, service life and safety of pumped storage power plants. (cf. Müller 2012; cf. Schleiss et al. 2010)

Globally, the average sedimentation rate of artificial reservoirs is estimated at around 0.8 % per year. The replacement investment of this annually lost storage capacity amounts to around 22 - 33 trillion US dollars per year[1]. It is also predicted that global warming will further intensify the problem of sedimentation. This is due to the fact that more intensive precipitation and larger areas without vegetation with erodible soil will increase the sediment input into rivers and therefore also into the storage basins. (cf. Schleiss et al. 2010)

A current example of this can be seen at the pumped storage power plant in Säckingen operated by Schluchseewerk AG. This power plant takes water from the Rhine and directs it into the artificially created Eggberg basin, which has a volume of 2.1 million m³. Over the years, the basin has filled up with fine sediment from the Rhine, restricting the regular operation of

[1] Adjusted for inflation of the US dollar from 2001 to 2024

the pumped storage power plant. After 130,000 m³ of sediment had already been removed from the basin in 1992, this step had to be carried out again in 2019 for 75,000 m³ of sediment. The sediment removal in 2019 was combined with a renovation measure and cost a total of nine million euros. (cf. Schluchseewerk AG 2023; cf. Schütz 2019)

In order to be able to operate pumped storage power plants effectively and sustainably in the long term and to meet the increasing requirements for storing large quantities of electricity, as well as providing peak energy and maintaining the frequency of the electricity grid, it is of great importance to develop measures to counteract the problem of sedimentation. Understanding the hydraulic processes that influence the sedimentation is fundamental to finding measures.

## 1.2 Aims

The aim of this study is to investigate the flow patterns of a pumped storage basin during pumping and turbine operation with model tests in the laboratory using Particle Image Velocimetry. This serves the purpose of creating a basis for numerical flow simulations of the sediments in these upper basins. The model experiments will take place at the Ujigawa Open Laboratory of Kyoto University in Japan.

The following research questions are to be answered:

- Why do sediment deposits occur in pumped storage basins?
- What is Particle Image Velocimetry (PIV) and how can it be used to capture flow patterns in the model?
- What do the flow patterns in an upper basin look like in the model during turbine or pump operation?

# 2 Basic principles

## 2.1 Pumped storage power plants

Pumped storage power plants have become increasingly important in recent decades. This is due to the fact that they allow large amounts of electrical energy to be stored with a high degree of efficiency ($\eta$ > 0.8 in modern plants) and released again within a very short time when required. They therefore play an important role in regulating the electricity grid and providing peak energy, particularly with regard to the advancing energy transition, as already described in chapter 1.1. However, pumped storage power plants are subject to a certain loss of volume due to sedimentation in the upper basin, which impairs the efficiency of the power plants. (cf. Mohringer 2022; cf. Müller 2012)

In this chapter, the structure, the sedimentation problem and previous solution approaches against sedimentation in pumped storage power plants will be explained in greater detail.

### 2.1.1 Structure

Pumped storage power plants usually consist of two water reservoirs at different altitudes, between which the water is moved back and forth through a headrace tunnel. To store electricity, water is pumped from the basin at a lower altitude into the basin at a higher altitude. Accordingly, electrical energy is converted into potential energy for the electricity storage process. To retrieve this potential energy, the water is led from the upper basin into the lower basin, where it passes through a turbine that generates electricity which can be fed into the power grid. (cf. Müller 2012)

In general, a river, natural lake or artificial basin serves as the lower basin. The upper basin usually consists of an artificial basin or, in alpine regions, a reservoir with a dam. (cf. Mohringer 2012)

A more detailed description of the general structure and characteristics of pumped storage power plants will not be provided here. If required, further information can be found in the literature by Giesecke et al. (2014), Mohringer (2012) and Müller (2012). However, as the intake and outlet structures are of particular importance in this study with regard to the model planning in chapter 3.1, they will be explained in more detail in the following paragraphs.

Inlet and outlet structures are structures in the upper and lower basin of a pumped storage power plant that are used for water intake and discharge. They are designed as a widening of the continuing headrace tunnel. During water intake, these structures act as a diffusor (gradual deceleration of the water) and during water discharge as a confusor (gradual acceleration of the water). In most cases, there is a single structure in the upper and lower basin each, which both serves as an inlet and outlet structure. Figure 2.1 shows a sketch of such a structure in plan view. (cf. Mohringer 2022)

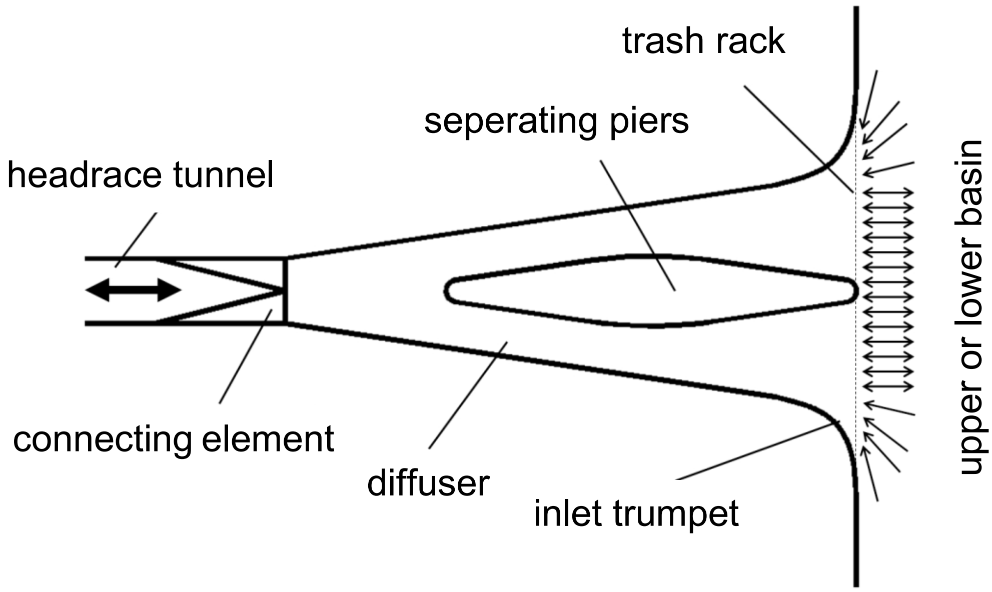


Figure 2.1 – Sketch of the inlet and outlet structure of a pumped storage power plant, top view (adapted from Mohringer 2012)

The diffuser forms the core of an inlet and outlet structure. The widening of the cross-section causes a reduction in the flow velocity of the water when water is introduced, which results in an increase in pressure. This process is known as pressure recovery and serves to reduce hydraulic losses. The higher the pressure increase in the structure, the lower the existing hydraulic losses. During water extraction, the diffuser acts as a confusor and increases the flow velocity of the water due to the narrowing of the cross-section. As a result, the accelerated flow is less prone to the formation of flow separations, which would cause hydraulic losses. (cf. Mohringer 2012)

The connecting element is used to connect the headrace tunnel, which is usually round, with the inlet and outlet structure, which generally has a rectangular cross-section. Separating piers are static elements to support the structure ceiling. However, they can also have a hydraulic effect by aligning the flow when water is discharged, thus creating a more homogeneous outflow into the subsequent upper or lower basin. The trash rack is used to separate coarse debris in the water, such as branches or stones, before it enters the intake structure. The inlet trumpet is a cross-section expansion directly at the adjacent basin. The opening angle is just large enough to ensure that controlled flow separation occurs when water is discharged, while no flow separation occurs when water is withdrawn. (cf. Mohringer 2012)

### 2.1.2 Sedimentation problematics

The loss of volume due to sedimentation in artificial reservoirs is a challenge whose significance will continue to increase in the coming years. This affects all artificial reservoirs that are used to store water. In addition to reservoirs for the supply of drinking water or flood protection, this also includes the upper and lower basins of pumped storage power plants. As the focus of this study is on the upper basins of pumped storage power plants, the sedimentation problem for this type of storage basin is discussed below.

In upper basins that have a natural inflow in addition to the headrace tunnel, sedimentation of the basin occurs due to the interruption of the balance between the input and output of sediment. There is a difference in density between the inflowing water with a high sediment concentration and the water already in the basin with a lower sediment concentration. As a result, the inflowing water flows along the bottom of the basin to the lowest point of the basin, which is usually located near the inlet and outlet structure. The sediment settles there due to the low flow velocities. This phenomenon is known as "turbidity current" and is the main source of sedimentation in alpine pumped storage power plants. (cf. Jenzer Althaus et al. 2008; cf. Müller et al. 2013b)

Upper basins of all types, whether with or without a natural inflow, experience sedimentation during pumping operations due to sediment input from the lower basin. Lower basins usually have a natural inflow and therefore sediment input as described in the previous paragraph. During pumping operations, the sediment, mainly suspended particles, is transported from the lower basin into the upper basin and settles there due to the low flow velocities and - in some cases - long retention times. (cf. Müller 2012)

This sediment input, whether from natural inflow or from the lower basin, has the effect of reducing the storage volume of the upper basin over time. The reduced usable volume also decreases the total amount of energy that can be stored, which impairs the pumped storage power plant's ability to provide peak power and regulate the power grid. Sediment deposits at the inlet and outlet structure can restrict their functionality or block them completely, which poses a safety risk with regard to the operation of the pumped storage power plant and flood protection. In addition, a high concentration of sediment in the water increases hydroabrasive wear on pumps, turbines and the lining of the headrace. Figure 2.1 shows a Francis impeller destroyed by hydroabrasion, which had to be completely replaced after only 10,000 operating hours due to the high concentration of suspended particles in the water. (cf. Jenzer Althaus et al. 2008; cf. Ortmanns 2006)

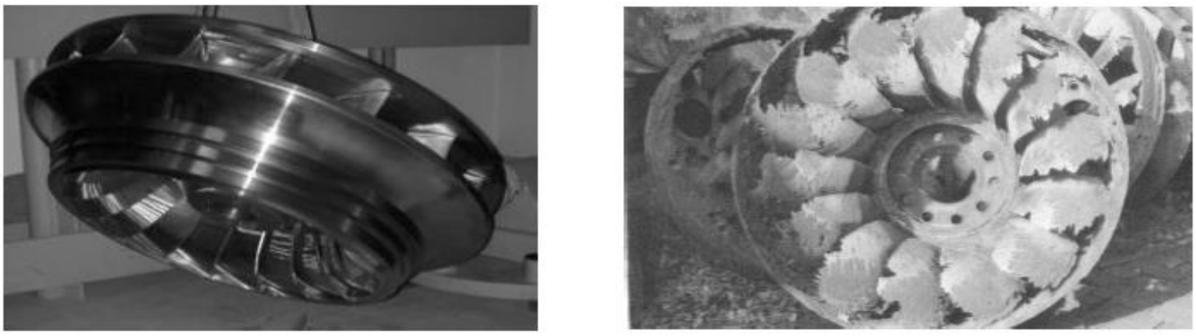

Figure 2.2 - Francis impeller as good as new (left) and destroyed by hydroabrasion (right) (Ortmanns 2006)

In addition, global climate change will continue to intensify the problem of sedimentation in basins. The sediment input into these basins essentially depends on the erosion characteristics in the catchment area. Soil erosion is expected to increase significantly in many areas as a result of global warming. This is partly due to progressive desertification and an increase in extreme precipitation events. Studies by Schleiss et al. (2010) predict that 80 % of the usable volume for hydropower in Europe will have been lost to sedimentation by 2080. In Asian countries, this is expected to occur as early as 2035. This makes it clear that the problem of sedimentation is affecting sustainable energy production on a large scale. (cf. Schleiss et al. 2010)

### 2.1.3 Solution approaches

The problem of sedimentation in reservoirs has been known for some time, which is why there is a large number of literature sources that present solutions to prevent sedimentation. Schleiss and Oehy (2002), for example, have compiled and documented conventional measures to prevent the sedimentation of reservoirs. These are primarily designed for reservoirs in alpine regions, but can also be applied to a certain extent to the upper basins of pumped storage power plants. (cf. Schleiss et al. 2010)

The measures are divided into preventive and retroactive measures. Preventive measures serve to prevent sediments from entering the water body and retroactive measures serve to subsequently remove sedimentation. Furthermore, a distinction is made between measures in the catchment area, in the reservoir and at the dam. The measures are shown in Figure 2.3 and can be found in Schleiss and Oehy (2002) for further information.

Additionally, the DWA (Deutsche Vereinigung für Wasserwirtschaft, Abwasser und Abfall e.V.) provides a detailed description of retroactive measures in its report from 2006. It explains different methods and procedures for removing sediment from reservoirs and discusses them with regard to ecological aspects. (cf. DWA 2006)

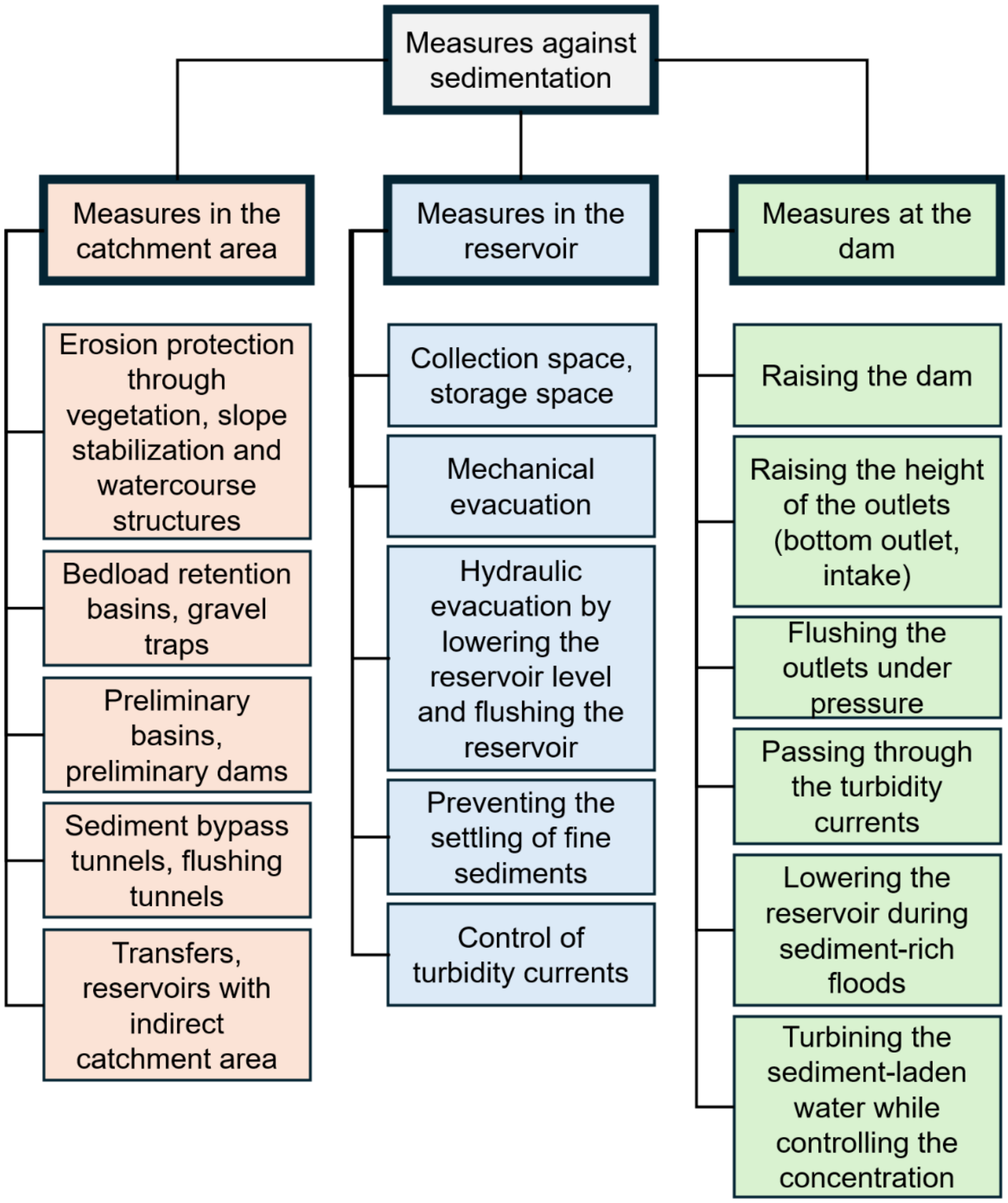


Figure 2.3 - Overview of preventive and retroactive measures against sedimentation (adapted from Schleiss and Oehy 2002)

As this study concentrates on the investigation of basic flow patterns in the upper basins of pumped storage power plants and not on the development and evaluation of measures to prevent sedimentation, the solution approaches will not be discussed in further detail here. More information regarding this topic can be found in the literature by Schleiss and Oehy (2002) and the DWA (2006).

## 2.2 Particle Image Velocimetry

Shallow flows mainly show flows in the vertical level. They are shallow flows if the vertical dimensions of the flow volume are significantly smaller than the horizontal dimensions. Most lakes, reservoirs, rivers and coastal areas belong to this category. The model of the upper basin, which is examined in this study, also belongs to this category. In order to investigate the flow patterns in such basins, the flow velocities must be recorded over the entire surface area. (cf. Kantoush and Schleiss 2009; cf. Vreugdenhil 1994)

A variety of methods have been available for recording flow velocities for some time, such as pitot-static tubes or hot-wire anemometers. However, the problem with these methods is that they have to be submerged into the flow to measure the velocity and therefore have an influence on it. In addition, these methods only measure the flow velocity at a specific position and are therefore unsuitable for recording large-scale flow patterns. A far more suitable method was developed in the 1970s and is known as Particle Image Velocimetry (PIV). (cf. Abdulwahab et al. 2022)

The PIV measurement method is based on applying tracer particles, referred to as seeding, to the flow under investigation. This seeding is illuminated by a strong light source, such as a laser sheet. A camera is used to record the movement of the seeding in the flow. Since the time interval between two frames of the recording is known and the change in position of the particle can be determined from the images, it is possible to calculate the flow velocity and direction. The advantage of this measurement method compared to the methods mentioned in the previous paragraph is that it is an indirect measurement, which means that the flow is not influenced by the measurement. Furthermore, with PIV it is possible to simultaneously record several flow velocities over a large area and is therefore well suited for measuring the flow patterns in a model of an upper basin of a pumped storage power plant, as will be conducted in this study. (cf. Raffel et al. 2018)

A special form of PIV is the so-called surface PIV. The main difference to the PIV described in the previous section is that with surface PIV, only the flow velocities and flows on the surface of the fluid under investigation are recorded. For this purpose, a light source is used that mainly illuminates the fluid surface and the seeding particles do not float in the fluid itself, but on the surface of the fluid. As the flow in this study is a shallow flow, the surface PIV method is used to record the flow patterns in the model basin. (cf. Raffel et al. 2018)

### 2.2.1 Components

In order for a flow velocity measurement to be carried out with a PIV system, a number of typical test components usually need to be defined. These consist of the seeding, the lighting and the recording equipment. In this chapter, these components will be described in summarized form.

The choice of seeding that is placed in the flow to record the change in position of the flow over time is of particular importance in PIV. The particles must be large enough to reflect enough light to be detected by the camera. At the same time, the particles must not exceed a certain size so that their movement accurately represents the flow. Another property to consider is the particle density. To ensure that the particles move with the flow and do not settle, the particle density should be similar to the water density. If a surface PIV is being conducted and only the surface flow velocities are to be measured, the particle density should be slightly lower than the water density so that the particles float on the water surface. Table 2.1 shows a list of suitable seeding materials for flows in liquids. (cf. Kantoush and Schleiss 2009; cf. Raffel et al. 2018)

Table 2.1 - Seeding materials for liquid flows (Raffel et al. 2018)

| Type | Material | Mean diameter [mm] |
|---|---|---|
| Solid | Polystyrene | 0,010 – 0,100 |
| | Aluminium flakes | 0,002 – 0,007 |
| | Hollow glass spheres | 0,010 – 0,100 |
| | Granules for synthetic coatings | 0,050 – 0,500 |
| Liquid | Different oils | 0,050 – 0,500 |
| Gaseous | Oxygen bubbles | 0,050 – 1,000 |

Lastly, the amount of the seeding particles must be determined. Depending on the amount of particles, different flow velocity measurements are performed. These are listed below and demonstrated in Figure 2.4.

a) Low particle amount: Particle Tracking Velocimetry (PTV)
   - Tracking of individual particles over multiple frames possible
b) Medium particle amount: Particle Image Velocimetry (PIV)
   - Individual particles can still be detected, but can no longer be tracked
c) High particle amount: Laser Speckle Velocimetry (LSV)
   - Individual particles can no longer be detected

Studies by Kantoush and Schleiss (2009) have shown that the particle amount in PIV tests should be set so that there are at least five particles in the interrogation area. The interrogation area is an aspect of the result evaluation and is explained in more detail in chapter 2.2.2. The particles can also be coated with paint. This reduces the force of attraction between the particles and therefore prevents agglomeration. (cf. Kantoush and Schleiss 2009)

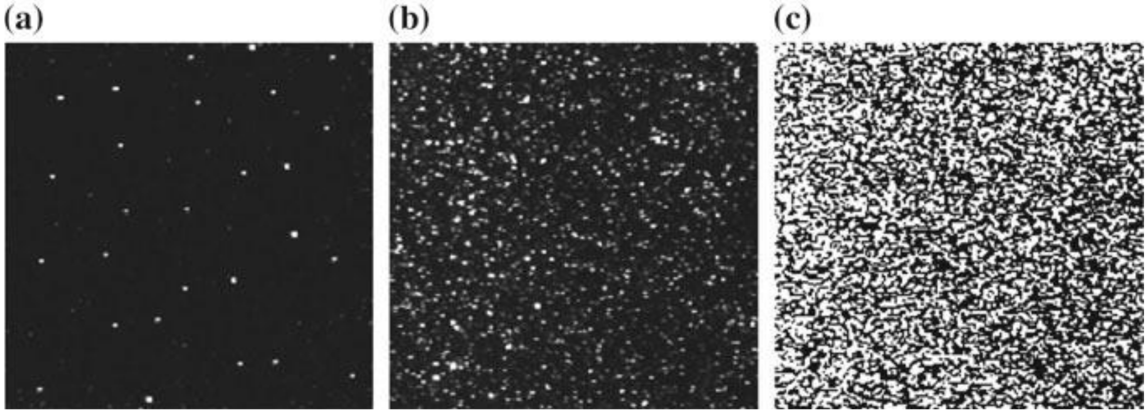


Figure 2.4 - The three modes of particle image density: (a) low (PTV), (b) medium (PIV), and (c) high image density (LSV) (Raffel et al. 2018)

The illumination in a PIV experiment has the function of highlighting the input particles in a plane or volume of the flow so that the camera can record the light reflected by the particles. For PIV experiments in water, continuous wave lasers are usually selected for this purpose. In contrast to pulsed lasers, this type of laser emits a light wave of constant intensity. However, if pulsed lasers are chosen, it is important to ensure that the exposure pulse is short enough to "freeze" a particle in its movement in order to avoid blurred images of the particle. The time difference between the exposure pulses should be large enough to record a change in position of the particle. Lasers have the advantage that they can emit monochromatic (single color) light with high energy density in thin layers without causing chromatic aberration (different degrees of refraction of light of different colors). (cf. Raffel et al. 2018; cf. Voss-de Haan 2000)

Light Emitting Diodes (LEDs) are another option for illumination. Through the development in recent years, LEDs have greatly increased in output power and efficiency and can therefore also be used for PIV experiments. LEDs have the advantage compared to lasers that they are easy to use, robust and, depending on the strength of the LEDs, pose a lower risk of injury. (cf. Raffel et al. 2018)

Regardless of the exposure apparatus, it is important to ensure that the light intensity is distributed homogeneously over the entire surface of investigation. Otherwise, reflections and shadows will occur, which could falsify the results of the PIV. It is also important to avoid backlighting. This can be achieved by switching off or dimming interfering light sources or by using a filter that corresponds to the wavelength of the laser or LEDs. (cf. Kantoush and Schleiss 2009)

PIV imaging methods can be divided into two categories. On the one hand, single-frame/multi-exposure PIV, in which one image shows the illuminated particles at several points in time, and on the other hand, multi-frame/single-exposure PIV, which provides several images and a separate particle distribution is recorded for each image. The main difference between the two imaging methods is that the single-frame approach does not provide any information about the temporal sequence of the particle images without additional effort. The steps required to obtain this information can be found in detail in Raffel et al. (2018). However, as there are nowadays very powerful cameras that allow images to be captured in very rapid succession, the multi-frame approach is now mainly used. This is also the case in this study. (cf. Raffel et al. 2018)

For the recording itself CCD (charge-coupled device) or CMOS (complementary metal oxide semiconductor) based digital cameras are suited. A detailed description of the camera technology and time control can also be found in Raffel et al. (2018). But time control is mainly important for PIV recordings with gaseous media and will therefore not be discussed further in this study. (cf. Raffel et al. 2018)

### 2.2.2 Evaluation of results

Once images from such a PIV test are available, the results can be analyzed. Before the flow velocities can be calculated from the images, orthorectification must be carried out. This applies in particular to recordings for large-area PIV tests (LSPIV), as in most cases a wide-angle lens is required in order to be able to record the flow area with a single camera. However, these wide-angle lenses create a distortion on the recorded images. As a result, straight lines are displayed as curves and the flow velocity cannot be calculated correctly. Orthorectification uses control points with known coordinates in the field of the image so that software can use these points for orientation and remove the distortion. Suitable software for this procedure includes the fee-based "PTLens", developed by Thomas Niemann, or "Fudaa-LSPIV" developed by Le Coz et al. (2014), which can be used free of charge. The result of an orthorectification for a wide-angle image can be seen in Figure 2.5. (cf. Kantoush and Schleiss 2009)

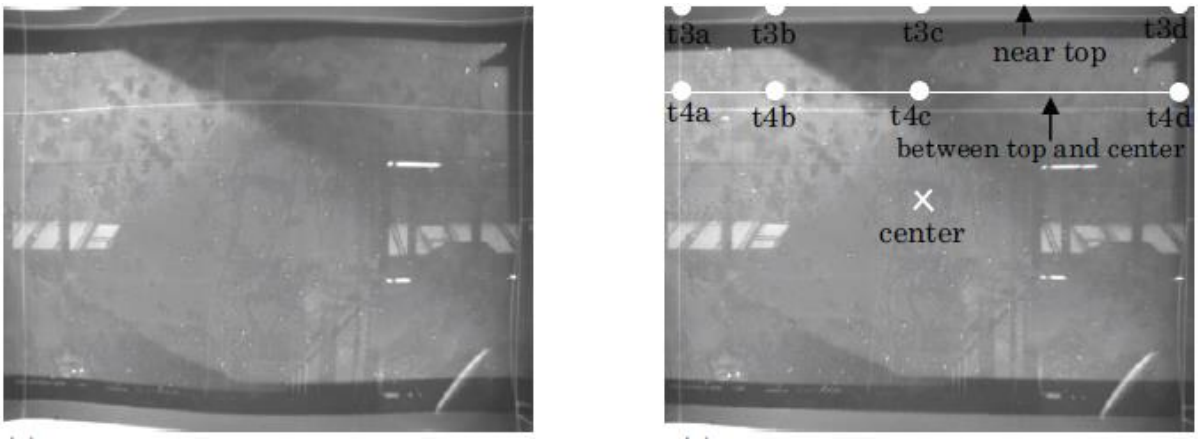


Figure 2.5 - Left: distorted image; right: corrected image with the control points by PTLens (Kantoush and Schleiss 2009)

The flow velocities and directions can then be calculated from the undistorted images in order to visualize the flow pattern of the basin or body of water under investigation. For this so-called evaluation, the recorded images are divided into several small sub-areas. These areas are referred to as interrogation areas (IA). A searching area (SA) is defined for the IA, in which the IA can move for particle identification. By cross-correlation, local displacement vectors are formed in these areas by the change in position of the seed particles and the known time interval between two consecutive images. With these vectors it is possible to determine velocity vectors. (cf. Raffel et al. 2018)

The choice of the size of the IA is important so that the calculation of these vectors can be carried out optimally. If the IA is too small, the flow velocity calculation can be inaccurate. Choosing an area that is too large leads to unnecessarily long calculation times. Research by Sutarto (2015) has shown that a size of 80 pixels for the IA provides good results. The SA should be so large that there is a distance of five to ten pixels between the edges of the two areas. A larger distance should be selected in the main flow direction. Figure 2.6 shows such a surface with its labeling. Suitable software for this calculation includes the Matlab-based program "RIVeR", developed at the Center for Water and Technology (CETA) at the National University of Córdoba, or the aforementioned "Fudaa-LSPIV". (cf. Patalano et al. 2017; cf. Sutarto 2015)

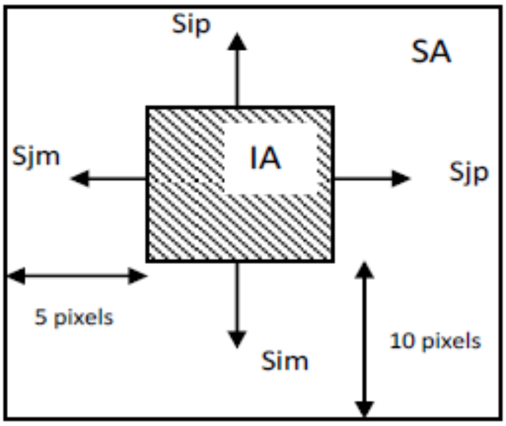


Figure 2.6 - Searching area, SA, and interrogation area, IA (Sutarto 2015)

After automatic calculation of the velocity vectors, large amounts of data are generated, which in most cases require further editing. This is referred to as post-processing and software such as that mentioned in the previous section can perform this. Only some of the post-processing procedures will be described in this paper; others can be found in Raffel et al. (2018).

An important post-processing method is the correction of raw data. This involves searching for obviously incorrect velocity vectors from the result files and removing them or replacing them with approximate values. With small amounts of data, this can be done manually. Otherwise, the use of software is necessary. Another process is data reduction. Result files often contain several hundred or thousand velocity vector fields that require many gigabytes of storage space. For efficient storage and processing of the data, the amount of data can be reduced by averaging. Finally, the presentation and animation of the data is an important aspect so that information can be obtained quickly and easily from the results. Some features that allow this are contour plotting, surface rendering or color coding and can be created with the software already mentioned. (cf. Raffel et al. 2018)

### 2.2.3 Uncertainties

The overall uncertainty of measurement results in PIV results from the combination of several possible causes of error. Errors can arise from a variety of steps that are necessary for the PIV process, ranging from test setup to test execution and results evaluation. Some of these errors and how to avoid them are described in the following paragraphs.

When conducting the experiment, errors can occur during the recording, which is strongly dependent on the selected seeding. If the particles are selected too large or with an unsuitable density, this can lead to these particles not correctly reflecting the movement of the flow. If the seeding is too small, this can lead to difficulties in focusing the particles with the camera during the recording. If either of these two sources of error occur, adjusting the seeding material can be a useful approach to reduce measurement errors in the following evaluation. (cf. Kantoush and Schleiss 2009)

An error that can occur during the evaluation of the recording is if the number of particles per interrogation area is not sufficient for a calculation by software. In chapter 2.2.1, the minimum number of particles per interrogation area was already set at five. If this is not achieved during the recordings, it may be helpful to increase the number of particles added or to use a mechanical feeder that evenly feeds the particles into the flow if they are not already being added in this way. (cf. Raffel et al. 2018)

In addition to the sources of error mentioned here, there are many other possibilities that can lead to uncertainties in the PIV result. However, describing all of these would go beyond the scope of this study. Further information regarding this topic can be found in the literature by Abdulwahab et al. (2022), Kantoush and Schleiss (2009) and Raffel et al. (2018).

## 2.3 Model laws

The investigation of the flow patterns of an upper basin of a pumped storage power plant does not have to be carried out in a real upper basin but can be simulated in a hydraulic model. A hydraulic model is a scaled-down replica of a real structure, the so-called prototype. Hydraulic models are physical models in which the measurable physical events are similar to those in the prototype. However, in order for this similarity to be achieved, there are a number of rules to be applied. These rules, their application limits and what happens if the rules are not applied will be the subject of the following paragraphs. (cf. Martin and Pohl 2000)

### 2.3.1 Mechanical similarity

A similarity between the hydraulic model and the prototype exists if the geometric, kinematic and dynamic parameters are in a specific relationship to each other. If this is the case, it is referred to as mechanical similarity between the model and the prototype. (cf. Martin and Pohl 2000)

The geometric similarity describes the similarity of the shape and is achieved when all geometric sizes, such as length, width and height, are transferred to the model with the same length scale number $\lambda_L$ of the prototype. The length scale number $\lambda_L$ is defined as follows:

$$\text{Length scale number } \lambda_L = L_{Prototype} / L_{Model} \tag{1}$$

The kinematic similarity describes the similarity of the motion of massless bodies and is described by the time scale number $\lambda_t$, which is valid for all time-dependent processes:

$$\text{Time scale number } \lambda_t = t_{Prototype} / t_{Model} \tag{2}$$

In dynamic similarity, all forces in a flow are in the same relationship between the prototype and the model. This refers to forces such as inertia, gravity, friction, capillarity, dynamic pressure and elasticity. The dynamic similarity is described with the force scale number $\lambda_F$:

$$\text{Force scale number } \lambda_F = F_{Prototype} / F_{Model} \tag{3}$$

If the criteria of these scale numbers are met, complete mechanical similarity is achieved. The criterion of dynamic similarity plays a particularly important role in hydraulic engineering testing, so that the flow in the model is similar to the flow in the prototype. However, with physical models it is not possible to achieve complete mechanical similarity between prototype and model. Although physical variables such as water density, gravitational acceleration or temperature generally remain the same, it is impossible to transfer more than two forces acting in the prototype to the model on an identical scale. This means that mechanical similarity is not achieved and scaling effects occur. (cf. Strobl and Zunic 2006)

### 2.3.2 Scaling effects

Scaling effects result from the fact that perfect mechanical similarity cannot be achieved. In hydraulic engineering models, these lead to differences between the observed flow phenomena in the prototype and in the model. As described in the previous section, dynamic similarity plays a particularly important role for the flow. For a better understanding of the scaling effects, Heller (2011) carried out studies on this and formulated four statements, which are summarized below.

First, it can be said that a hydraulic model always contains scaling effects if the scaling is not 1:1, as otherwise it is impossible to bring all force scale numbers into the same ratio. It is therefore relevant to determine whether the scaling effects that occur can be neglected or not. (cf. Heller 2011)

Furthermore, the larger the scale number, the greater the associated scaling effects. However, the decision as to whether the scaling effects that occur can be neglected is not dependent on the size of the scale number and the associated effect. (cf. Heller 2011)

The extent of the scaling effects also depends on the flow phenomenon or parameter being investigated, as the relative importance of the forces involved can differ. If a parameter is not significantly affected by scaling effects, this does not necessarily mean that other parameters in the same experiment are also not affected. An example of this is shown in the model test of the Gebidem Dam in Switzerland, which can be seen in Figure 2.7. The scaling here is at a scale of 1:30. The size of the flow is hardly affected by scaling effects. However, the amount of air entrainment differs greatly between the prototype and the model. (cf. Heller 2011)

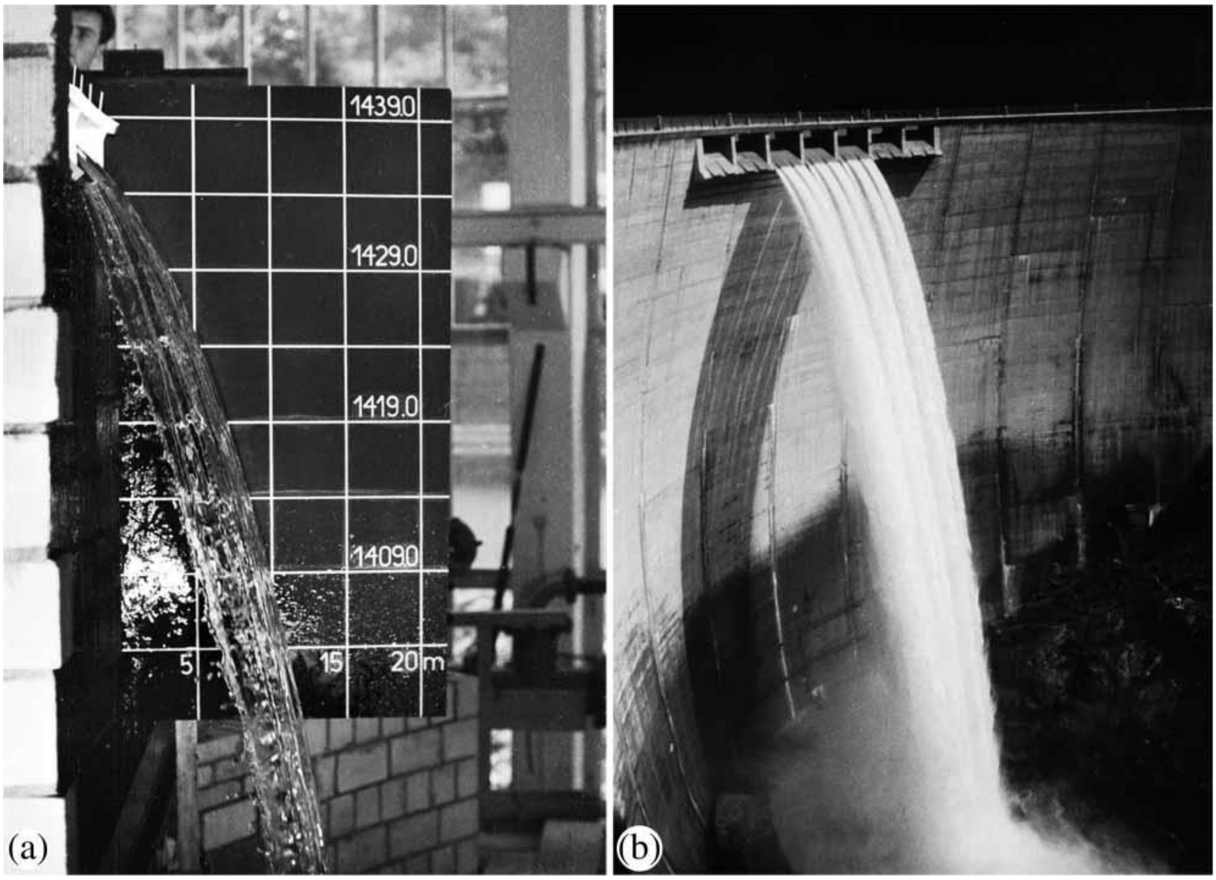


Figure 2.7 - Overflow spillway of Gebidem Dam, Valais, Switzerland: (a) physical hydraulic model at scale 1:30, (b) real-world prototype in 1967 (Heller 2011)

Lastly, the flow forces in a model are generally more dominant than in the real prototype. Therefore, scaling effects usually have a dampening effect on the flow phenomenon. This can also be seen in Figure 2.7 if the amount of air entrainment is examined, which is significantly lower in the model than in the prototype. (cf. Heller 2011)

As scaling effects distort the expected result of a model test, there are a number of procedures for managing them in practice. Rules of thumb are often applied in order to avoid scaling effects from the beginning. These rules describe scaling variables, dimensions and other properties of the model for a wide variety of model setups and investigated flow phenomena. These rules are shown in the Appendix 1.1.

Scaling effects can also be avoided by replacing the fluid under investigation. Very similar flow phenomena can occur in different fluids. An example of this is presented in Figure 2.8 which shows the similarities between the sediment morphology of sand in water and in air. (cf. Heller 2011)

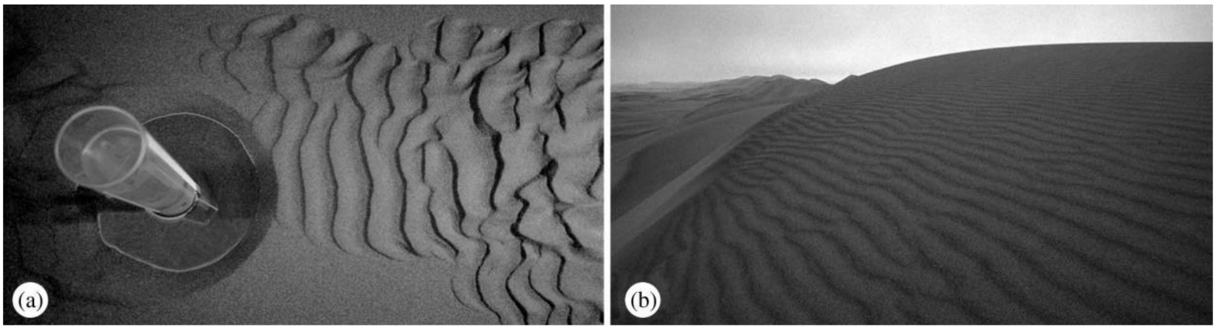


Figure 2.8 - Replacement of fluid: similar morphologies in sand caused by fluid (a) water and (b) air (Heller 2011)

Another option for dealing with scaling effects is compensation, which is achieved by distorting the model geometry. Disregarding the exact geometric similarity of some parameters can lead to an improved similarity between prototype and model. An example of this is the reduction of wall roughness by neglecting geometric similarity, which results in an identical friction coefficient between prototype and model and therefore leads to compensation of scaling effects. (cf. Martin and Pohl 2000)

The construction of a model that is too small with non-negligible scaling effects may be due to economic considerations, limited space or a lack of time. In this case, correction offers a measure for dealing with scaling effects. During correction, the model results are later modified so that they better match the investigated flow phenomenon. This adjustment is only possible if sufficient information about the quantitative influence of the scaling effects on the result is available. (cf. Heller 2011)

### 2.3.3 Laws of similarity

In most model investigations, not all hydraulic phenomena are of interest in the same way. Depending on the task, a decision must be made for the design of the model as to which of the types of forces (inertia, gravity, friction, capillarity, dynamic pressure and elasticity) are of secondary importance. This leads to a so-called "approximate dynamic similarity". In addition to the inertia force, which is practically always present due to the flow velocity in the prototype and in the model, a further influencing variable must be selected which is dominant in the flow process. (cf. Strobl and Zunic 2006)

There are a number of similarity laws that are used depending on the size of interest. These laws can be differentiated according to which two forces are transferred from the prototype to the model with the same scale. Table 2.2 lists the most important model laws. (cf. Strobl and Zunic 2006)

Table 2.2 - Model laws and the forces that in dominate them (adapted from Strobl and Zunic 2006)

| **Model law** | **Dominating force** |
|---|---|
| Froude | Inertia and gravity |
| Reynolds | Inertia and friction |
| Weber | Inertia and capillarity |
| Thoma | Inertia and dynamic pressure |
| Cauchy / Mach | Inertia and elasticity |

In hydraulic engineering experiments, inertia and gravity are the most dominant forces. This applies to most experiments with a free water level, as the frictional forces are negligible there. These include experiments with fully developed turbulence, flow over weirs, wave movements, still pools, surge and sink, flow in deep waters, but also pressurized pipe flows in hydraulically rough areas, where the influence of the Reynolds number is negligible. For this reason, Froude's law is used in most cases, where the Froude number always remains the same between prototype and model (sub-critical: $Fr < 1$ or super-critical: $Fr > 1$). Table 2.3 provides conversion aids for dimensioning a model according to Froude. (cf. Heller 2011; cf. Martin and Pohl 2000; cf. Schlurmann 2002; cf. Strobl and Zunic 2006)

Table 2.3 - Conversion aids for the dimensioning of a Froud model (adapted from Auel 2023)

| **Parameters** | **Dimension** | **Froude** |
|---|---|---|
| **Geometry** | | |
| Length | $L$ | $M_L$ |
| Surface area | $L^2$ | $M_L^2$ |
| Volumene | $L^3$ | $M_L^3$ |
| **Kinematic** | | |
| Time | $T$ | $M_L^{1/2}$ |
| Velocity | $LT^{-1}$ | $M_L^{1/2}$ |
| Acceleration | $LT^{-2}$ | 1 |
| Flow rate | $L^3T^{-1}$ | $M_L^{5/2}$ |
| **Dynamic** | | |
| Mass | $M$ | $M_L^3$ |
| Force | $MLT^{-2}$ | $M_L^3$ |

Another law that is more commonly used in hydraulic engineering experiments is Reynolds' law. Here, the Reynolds number always remains the same between the prototype and the model (laminar: $Re < 2320$ or turbulent: $Re > 2320$). This law is applied when inertial forces and frictional forces dominate the flow. This can be the case in experiments for intake structures or pipe flows in the hydraulically smooth range. Table 2.4 shows the conversion aids for dimensioning a model according to Reynold. (cf. Heller 2011; cf. Schlurmann 2002)

Table 2.4 - Conversion aids for the dimensioning of a Reynold's model (adapted from Auel 2023)

| Parameters | Dimension | Reynolds |
|---|---|---|
| **Geometry** | | |
| Length | $L$ | $M_L$ |
| Surface area | $L^2$ | $M_L^2$ |
| Volumene | $L^3$ | $M_L^3$ |
| **Kinematic** | | |
| Time | $T$ | $M_L^2$ |
| Velocity | $LT^{-1}$ | $M_L^{-1}$ |
| Acceleration | $LT^{-2}$ | $M_L^{-3}$ |
| Flow rate | $L^3T^{-1}$ | $M_L$ |
| **Dynamic** | | |
| Mass | $M$ | $M_L^3$ |
| Force | $MLT^{-2}$ | 1 |

A significant disadvantage of dimensioning according to Reynolds are the sometimes impractical scaling ratios, such as the flow velocity with the conversion $\lambda^{-1}$. A flow phenomenon with a flow velocity of 1 m/s in the prototype would result in a flow velocity of $v_{M,Re.}$ = 1 m/s * $25^{-(-1)}$ = 25 m/s in a model with a scaling of 1:25. In comparison, in a model according to Froude, the flow velocity would result in just $v_{M,Fr.}$ = 1 m/s * $25^{-1/2}$ = 0.2 m/s, which is much easier to be implemented in a model. (cf. Heller 2011)

### 2.3.4 Model limits

By disregarding individual influencing variables in order to achieve "approximate dynamic similarity", many compromises are sometimes necessary in the execution of the experiments. It is not possible to reduce or enlarge each model to any scale, as there are limits to the transfer from prototype to model. The most important limits include the turbulence limit, flow change limit, roughness limit, capillary limit, cavitation limit and aeration limit. In the context of this study, only the limits that are relevant for the planned experiment are discussed below. (cf. Martin and Pohl 2000)

The turbulence limit states that a turbulent flow on the prototype must also be reproduced in the corresponding model with a turbulent flow. The Reynolds number Re of a turbulent prototype flow must therefore not fall below the value of 2320 in the model, as otherwise it would be laminar flow. In such a case, the scale would not be valid and a different one would have to be chosen. Laminar flows can be achieved if the dimensions in the model are greatly reduced and therefore the flow velocity also decreases. In experiments in which the prototype is already close to the laminar range, this turbulence limit must be taken into particular consideration. (cf. Martin and Pohl 2000)

In addition to the classification of the flow state as laminar or turbulent, the flow state can also be classified as sub-critical or super-critical using the Froude number Fr. The transition from sub-critical to super-critical and vice versa is called flow change. The investigation of this threshold in a prototype and in a model proves to be difficult, as the smallest influences in the model can cause a change in the flow state. With the flow change limit, the aim is to achieve a definite flow state in the model that matches that of the prototype. Modeling with a Froude number close to one should therefore be avoided if possible. (cf. Martin and Pohl 2000)

Finally, the capillary limit may be of importance for the experiment conducted here. As the surface tension is strongly over-represented in a reduced model, the flow depths should not be too small. The rule of thumb in this case is that there should always be a sufficient water depth of at least 3 cm. (cf. Schlurmann 2002)

Other model limits such as the roughness limit, cavitation limit and aeration limit are not relevant for this study. This is due to the fact that the flow phenomena in which these boundaries are of particular importance, such as pipe flow, cavitation or free jets, are not investigated here. (cf. Martin and Pohl 2000)

# 3 Methodology

## 3.1 Model planning

The model planning process can be divided into several phases. First, various already existing upper basins of pumped storage power plants were considered, whereby different potential scales for different similarity laws were calculated. Practicable scales with associated similarity laws were then selected for model construction. In the next step, an inlet or outlet structure of a real upper basin was converted to the selected scale. This made it possible to develop upper basins for the selected scales which, although they do not exist in reality, are very closely based on existing upper basins and can be built as models at the same time. Finally, the relevant model limits for these basins were calculated to show that the selected scales are suitable. This allowed the basin designs to be sent to the responsible person at Kyoto University, who then commissioned the construction of one of these basins. The following chapters provide a detailed explanation of these steps.

### 3.1.1 Scaling of existing upper basins

The upper basins considered for the model planning are the Eggberg basin of the Säckingen pumped storage power plant operated by Schluchseewerk AG, the upper basin of the Markersbach pumped storage power plant operated by Vattenfall GmbH and the upper basin of the Goldisthal pumped storage power plant, also operated by Vattenfall GmbH. The dimensions, storage volumes and flow heights in pump and turbine operation were researched for these upper basins. This information was obtained from the websites of the individual pumped storage power plants and from Google Earth (Schluchseewerk AG 2023; Vattenfall GmbH 2023a, 2023b; Google LLC 2022).

These basins were then scaled down to different scales using Table 2.3 in accordance with Froude's law of similarity. This law of similarity was chosen because the experiments involved a free-surface flow in which the frictional forces are negligible due to the expected size of the basin. The results of this procedure are listed below for the upper basin of the Goldisthal pumped storage plant. The results for the other two basins under consideration can be found in the Appendix 1.2 and 1.3.

Due to the specific shape of the upper basin of the Goldisthal pumped storage power plant, an additional calculation of a rectangular basin equivalent in area and volume was carried out before applying different scales. The reason for this was that the model basin is also to be rectangular in shape and therefore a better comparability can be achieved. This step was not necessary for the other upper basins, as they already have an approximately rectangular shape.


Figure 3.1 - Satellite image of the upper basin of the Goldisthal pumped storage power plant of Vattenfall GmbH (Google LLC 2022)

The upper basin of the Goldisthal pumped storage power plant has an area of around 557,000 m² and a maximum storage volume of 13,000,000 m³ (cf. Google LLC 2022; cf. Vattenfall GmbH 2023a). From this, an average flow depth of $h_p$ = 23.34 m can be calculated. As the area of the basin is the product of the basin length and basin width and it can be assumed that the basins are approximately twice as long as they are wide, a rectangular basin equivalent to the Goldisthal upper basin can be calculated from this. The assumption of the ratio of length to width comes from the upper basin of the Markersbach pumped storage power plant, which has a length of 990 m and a width of 450 m. From the calculation just described an area and volume equivalent basin with a length of 1056 m and a width of 528 m, as well as an average flow depth of 23.32 m is obtained. Several potential scales were calculated for this basin, which can be seen in Table 3.2. The amount of flow during turbine operation comes from Vattenfall GmbH (2023a). No information was provided for the flow during pump operation.

Table 3.1 - Properties of the equivalent rectangular basin to the upper basin of the Goldisthal pumped storage power plant

| Description | Abbreviation [Unit] | Value |
|---|---|---:|
| Length | $L_P$ [m] | 1056 |
| Width | $b_P$ [m] | 528 |
| Flow depth | $h_P$ [m] | 23.32 |
| Storage volume | $V_P$ [m³] | ~ 13,000,000 |
| Flow rate pump operation | $Q_{P,Pump.}$ [l/s] | No information |
| Flow rate turbine operation | $Q_{P,Turb.}$ [l/s] | 413,000 |

Table 3.2 - Scaling of the equivalent rectangular basin to the upper basin of the Goldisthal pumped storage power plant according to Froude's law of similarity

| **Scale** M [-] | **Length** $L_M$ [m] | **Width** $b_M$ [m] | **Flow depth** $h_M$ [m] | **Flow rate pump operation** $Q_{M.,Pump.}$ [l/s] | **Flow rate turbine operation** $Q_{M.,Turb.}$ [l/s] |
|---|---|---|---|---|---|
| 1:50 | 21.12 | 10.56 | 0.47 | - | 23.36 |
| 1:75 | 14.08 | 7.04 | 0.31 | - | 8.48 |
| 1:100 | 10.56 | 5.28 | 0.23 | - | 4.13 |
| 1:150 | 7.04 | 3.52 | 0.16 | - | 1.50 |
| 1:175 | 6.03 | 3.02 | 0.13 | - | 1.02 |
| 1:200 | 5.28 | 2.64 | 0.12 | - | 0.73 |
| 1:250 | 4.22 | 2.11 | 0.09 | - | 0.42 |
| 1:275 | 3.84 | 1.92 | 0.08 | - | 0.33 |

As it is possible that the Reynolds similarity law is more suitable at the inlet and outlet structures due to the frictional forces that occur, this scaling was also calculated for the upper basins under consideration. The calculation was carried out according to the data in Table 2.4. With this scaling, the impractical scaling ratios, as already described in chapter 2.3.3, make it noticeable that the flow rates become extremely high. This is due to the fact that in reality the pumped storage power plants have very high flow rates with correspondingly high turbulence and Reynolds' law of similarity sets out to achieve the same Reynolds number on the prototype and in the model. Therefore, scaling according to Reynolds is not possible for this model structure and the similarity law according to Froude is used. The results of this calculation for the upper basin of the Goldisthal pumped storage power plant can be seen in Table 3.3. The results for the Eggberg basin and the upper basin of the Markersbach pumped storage power plant can be found in the Appendix 1.2 and 1.3.

Table 3.3 - Scaling of the equivalent rectangular basin to the upper basin of the Goldisthal pumped storage power plant according to Reynold's law of similarity

| **Scale** M [-] | **Length** $L_M$ [m] | **Width** $b_M$ [m] | **Flow depth** $h_M$ [m] | **Flow rate pump operation** $Q_{M.,Pump.}$ [l/s] | **Flow rate turbine operation** $Q_{M.,Turb.}$ [l/s] |
|---|---|---|---|---|---|
| 1:50 | 21.12 | 10.56 | 0.47 | - | 8260 |
| 1:75 | 14.08 | 7.04 | 0.31 | - | 5507 |
| 1:100 | 10.56 | 5.28 | 0.23 | - | 4130 |
| 1:150 | 7.04 | 3.52 | 0.16 | - | 2753 |
| 1:175 | 6.03 | 3.02 | 0.13 | - | 2360 |
| 1:200 | 5.28 | 2.64 | 0.12 | - | 2065 |
| 1:250 | 4.22 | 2.11 | 0.09 | - | 1652 |
| 1:275 | 3.84 | 1.92 | 0.08 | - | 1502 |

Once the law of similarity had been defined, the scales were selected. It was crucial to choose a scale that was neither too high, leading to a very low discharge or laminar flow, nor too low to make the model technically and economically possible. Therefore, two scales were selected that fulfill these conditions: 1:175 and 1:275. These scales are further elaborated below.

### 3.1.2 Scaling inlet / outlet structure

The inlet and outlet structure plays an important role for the flow in the upper basin of a pumped storage power plant. For this reason, a correct representation and scaling of this structure in the model is also of great significance. The inlet and outlet structure of the Goldisthal pumped storage power plant was chosen as a reference for the model. Figure 3.2 shows this structure while it was still under construction.

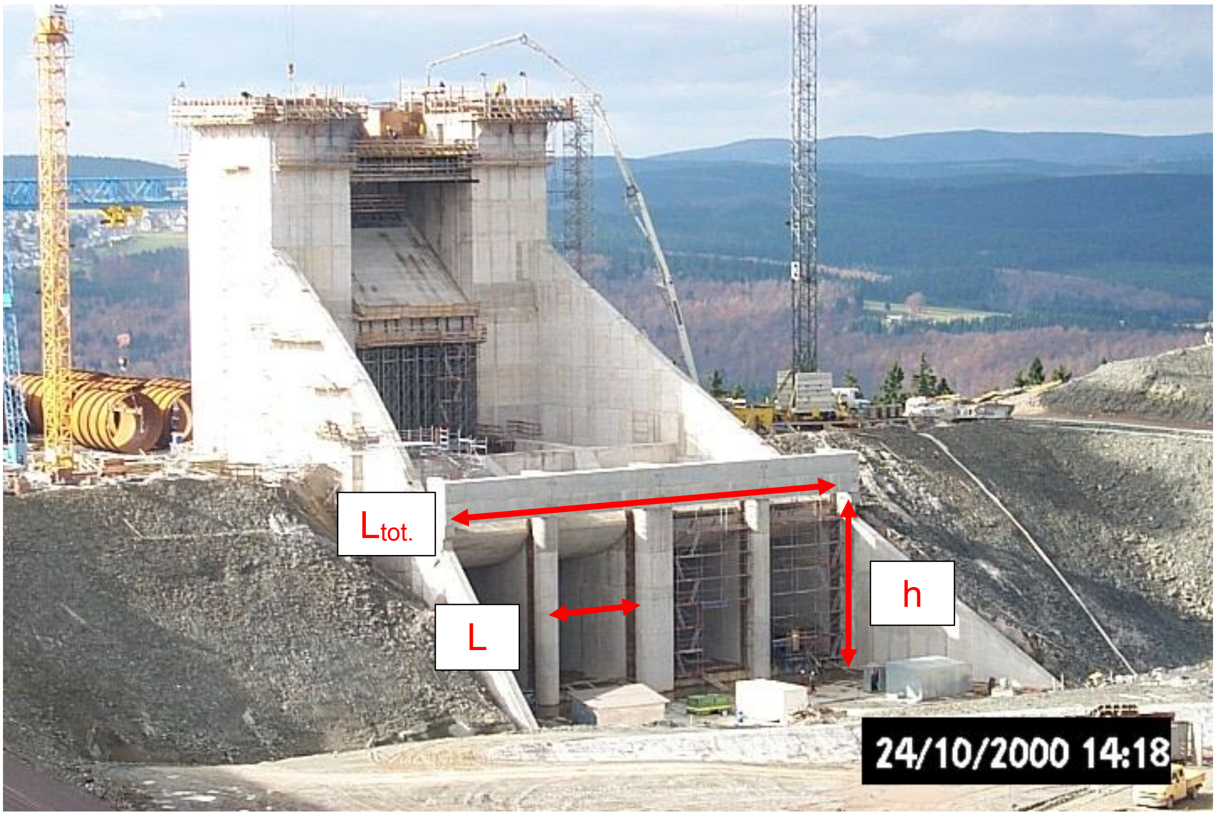


Figure 3.2 - Inlet / outlet structure at the upper basin of the Goldisthal pumped storage power plant during the construction phase (Clauss Ingenieure n. D.)

The dimensions of the inlet trumpet, which leads into the headrace tunnel, are of interest with regard to the model structure. These dimensions of the real structure were taken from the VDE Kassel (2006) and scaled down to model size using the above-mentioned scales. A sketch was also produced showing the structure of the inlet and outlet structure of the model. The results of this scaling are shown in Table 3.4, while the design sketch is shown in Figure 3.3.

Table 3.4 - Dimensions of the inlet/outlet structure in reality and selected scales (adapted from VDE Kassel 2006)

| Scale [-] | Total length $L_{tot.}$ [m] | Section length L [m] | Height h [m] |
|---|---:|---:|---:|
| 1:1 | 30.00 | 7.5000 | 15.000 |
| 1:175 | 0.17 | 0.0425 | 0.085 |
| 1:275 | 0.11 | 0.0275 | 0.055 |

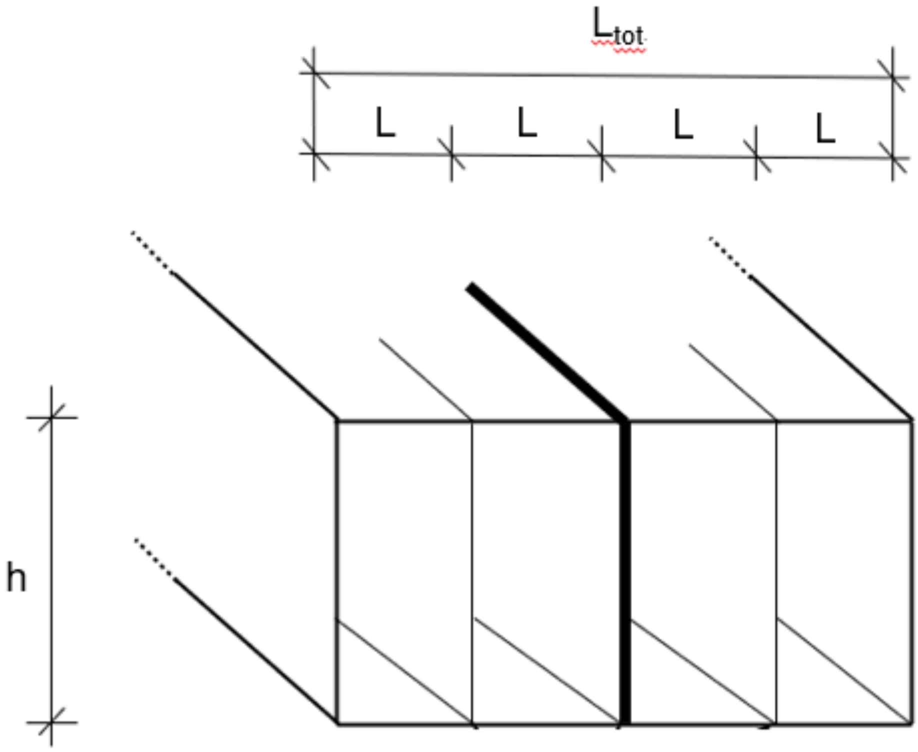


Figure 3.3 – Design sketch of the inlet and outlet structure in the model basin

### 3.1.3 Model basin design

In addition to the inlet and outlet structure, the actual model basin is also of importance for the flow patterns in the entire basin. The model basins considered for construction are not direct reproductions of one of the upper basins under consideration at the scales 1:175 and 1:275 as listed in Table 3.2 or in the Appendix 1.2 and 1.3. Instead, basins with dimensions based on the calculated scales were selected. This approach aims to achieve a balance between realism and practical implementation. The selected scales were kept, so that when the chosen model basins are scaled up, they represent upper basins of pumped storage power plants that are very similar to existing upper basins. The dimensions selected for the basins and the scaled-up dimensions for verifying realism are listed in Table 3.5 and Table 3.6.

Table 3.5 - Dimensions of the model basin at a scale of 1:175 and scaled up

| Description | Abbreviation [Unit] | M 1:175 | Upscaled basin |
|---|---|---:|---:|
| Length | L [m] | 5.00 | 875 |
| Width | b [m] | 3.00 | 525 |
| Flow depth | h [m] | 0.14 | 24.5 |
| Storage volume | V [m³] | 2.10 | ~ 11,000,000 |
| Flow rate pump operation | $Q_{Pump.}$[l/s] | 1.00 | 405,000 |
| Flow rate turbine operation | $Q_{Turb.}$[l/s] | 1.00 | 405,000 |

Table 3.6 - Dimensions of the model basin at a scale of 1:275 and scaled up

| Description | Abbreviation [Unit] | M 1:275 | Upscaled basin |
|---|---|---:|---:|
| Length | L [m] | 3.00 | 825 |
| Width | b [m] | 2.00 | 550 |
| Flow depth | h [m] | 0.09 | 24.75 |
| Storage volume | V [m³] | 0.54 | ~ 11,000,000 |
| Flow rate pump operation | $Q_{Pump.}$[l/s] | 0.32 | 401,000 |
| Flow rate turbine operation | $Q_{Turb.}$[l/s] | 0.32 | 401,000 |

The upscaled basins show a clear similarity to each other and to the real upper basins of the Säckingen, Markersbach and Goldisthal pumped storage power plants. The flow rates in the models are based on the flow rates of the Markersbach and Goldisthal pumped storage plants, as these are relatively high compared to the basin geometry. This is advantageous for the model basins as, according to Froude's law of similarity, the flow there is greatly reduced due to the scaling. Drawings were made to illustrate these model basins, which can be found in the Appendix 1.4.

### 3.1.4 Calculation model limits

After determining the scale and the model dimensions, it must be verified whether the model limits, which have already been described in chapter 2.3.4, are being exceeded and the scaling would therefore be invalid. This was carried out for the relevant model limits, which are the turbulence limit, the flow change limit and the capillary limit.

Checking the turbulence limit requires the calculation of the Reynolds number, which must not fall below the limit value of 2320 if the Reynolds number of the prototype is also above this limit, which indicates a turbulent flow area. The Reynolds number was determined at the inlet and outlet structure. The results of the calculations are summarized in Table 3.7, while the detailed calculations can be found in the Appendix 1.5.

Table 3.7 - Calculation of the Reynolds number in the prototype and model for checking the turbulence limit

| **Description** | **Abbreviation [Unit]** | **M 1:175** | **M 1:275** |
|---|---|---|---|
| Flow rate | Q [m³/s] | 405 | 401 |
| Surface area | A [m²] | 450 | 450 |
| Flow velocity | v [m/s] | 0.900 | 0.891 |
| Hydraulic diameter | $d_H$ [m] | 20 | 20 |
| Reynolds number prototype | $Re_{P.}$[-] | 17,964,071 | 17,786,649 |
| Reynolds number model | $Re_{M.}$[-] | 7,760 | 3,900 |

The table shows that the Reynolds numbers in the respective prototypes are well above the limit value and can therefore be clearly assigned to the turbulent flow state. Likewise, the Reynolds numbers of the models exceed the limit value of 2320 and are also in the turbulent flow range. This confirms that the turbulence limit condition is fulfilled.

Next, the flow change limit was examined, for which the Froude number had to be calculated. The critical value of the Froude number is one. If the Froude number is below one, the flow state is sub-critical and if it is above one, the state is described as super-critical. The condition to be fulfilled is that no different flow states occur in the prototype and in the model, which can be the case with models according to Froude's law of similarity if the Froude number of the prototype is close to the critical value. The calculations were also carried out on the inlet and outlet structure and the results are summarized in Table 3.8. The detailed calculation steps can again be found in the Appendix 1.6.

Table 3.8 - Calculation of the Froude number in the prototype and model for checking the flow change limit

| **Description** | **Abbreviation [Unit]** | **M 1:175 (Prototype)** | **M 1:175 (Model)** | **M 1:275 (Prototype)** | **M 1:275 (Model)** |
|---|---|---|---|---|---|
| Flow velocity | v [m/s] | 0.900 | 0.070 | 0.891 | 0.053 |
| Flow depth | h [m] | 5.250 | 0.030 | 8.250 | 0.030 |
| Froude number | Fr [-] | 0.125 | 0.129 | 0.099 | 0.098 |

The results show that the Froude numbers are well below the critical value. This means that both the prototypes and the models are in a sub-critical state and the flow change limit is fulfilled. In addition, the almost identical Froude numbers in the prototype and in the model serve as a verification of the correct scaling according to Froude's law of similarity, as these should be the same for such a model.

Finally, the capillary limit was verified. To achieve this, the flow depths in the model should be at least 3 cm in order to avoid an excessive influence of surface tension. The maximum flow depths at the scales 1:175 (14 cm) and 1:275 (9 cm) fulfill this limit. To ensure that the capillary limit is also met at minimum flow depth, the minimum flow depth is set at 3 cm for both models. Attempts below this flow depth were avoided.

The creation of the model basins was therefore completed and the designs were sent to the responsible person at Kyoto University for construction. This person decided to choose the scale of 1:275 due to limited space availability and economic reasons. A drawing of the final version of the model basin at a scale of 1:275 can be found in the Appendix 1.7.

## 3.2 Experimental setup

At the beginning of the experiments at the Ujigawa Open Laboratory, there were no extensive studies with surface PIV systems. Therefore, this study required additional effort to optimize the experimental setup to adequately capture the flow patterns in the model. In the following, both the original and the final experimental setup are explained, with the original setup presented in a summary. A detailed explanation of the optimization measures can be found in chapter 4.

### 3.2.1 Original setup

The model consists of a steel frame that encloses a wooden basin. To ensure that the wooden basin is watertight, it was coated with water-repellent paint. The inlet and outlet structure is located on one of the shorter sides of the rectangular basin and leads into the basin through a hole in the wooden wall. This structure is made of Plexiglas, connected to the basin and also treated with water-repellent paint at the connection point.

A pipe with a junction leads from the outlet structure: One end of the junction leads into a second, deeper basin, which serves as a water reservoir into which the water flows, driven by gravity, during the turbine operation. An actual turbine or pump that pumps the water out of the basin has not been installed. Before entering the storage basin, the water passes through a collecting net that serves to catch seeding particles from the outflowing water. A pump is installed at the other end of the junction, which can pump the water from the storage basin back into the main basin. The pipes branching off can each be shut off or opened with a valve. The exact dimensions of the basins and the inlet and outlet structure can be found in the Appendix 1.7. The pump used is the "Minipondy KP-401" from "Koshin Ltd. This part of the test setup remains unchanged in the final version and can be seen in Figure 3.4.

The components that were replaced during the experiments include the seeding particles used as well as the exposure, the camera and its mounting. The seeding particles initially used are listed in Table 3.9. Images of the individual seeding materials can be found in the Appendix 1.8. As most of these materials are not intended for use in scientific laboratory experiments, no product data sheets were available for further properties of the material.

Table 3.9 – First used seeding materials

| **Seeding** | **Mean diameter [mm]** |
|---|---|
| Charcoal (fine) | 0,032 – 0,042 |
| Charcoal (coarse) | 1,000 – 3,200 |
| Crushed Walnutshells | 0,500 – 2,000 |
| Rice husk | 0,200 – 4,000 |

The basin was illuminated by the fluorescent lamps on the ceiling of the room in which it was positioned. The camera used was a "Handycam HDR-CX520" of the brand "Sony". It was placed on a tripod in the basin and aimed down towards the sole of the basin.

### 3.2.2 Final setup

As previously mentioned, the model basin itself, the inlet and outlet structure, the storage basin and the pump correspond to the original setup and are therefore not described further here.

During several tests, it became apparent that the seeding materials listed in Table 3.9 were not suitable for the surface PIV tests. Therefore, additional materials were tested, which are listed in Table 3.10. Of these, the seeding material "Cork" proved to be the most suitable, which is why it was used for the further PIV recordings. Images of these materials can also be found in the Appendix 1.8.

Table 3.10 – Further used seeding materials

| **Seeding** | **Mean diameter [mm]** |
|---|---|
| Polystyrene Beads | 3,000 |
| Polyethylene Beads („Ironing Beads“) | 2,000 – 3,000 |
| Cork | 1,000 – 3,000 |

The final test set-up was illuminated by two standing spotlights, which were positioned centrally on the longer sides of the basin. Each spotlight had two lamps, each of which were directed towards the opposite corners of the model basin to ensure uniform illumination. The water was colored white with a bath additive to prevent the seeding particles from forming shadows on the basin floor.

The tests were recorded with the "Hero 12" camera from "GoPro". The recordings were made in 4K resolution at 30 frames per second with a wide-angle lens with a lens size of 16 - 34 mm. The camera was attached to the center of the ceiling above the model basin using a suction cup mount. Due to the strong distortion of the recordings by the wide-angle lens of the camera, measuring tapes were placed along the long sides of the basin, which served as reference points for the later orthorectification of the video recordings using software.

At last, a marking was placed on the edge of the basin, on the opposite side of the inlet and outlet structure, to track the approximate water level in the basin during the recording. The marking can also be used to see whether water is being pumped into the basin and the water level is increasing or whether water is flowing out and the water level in the basin is decreasing. This tracking was carried out because it makes it possible to not analyze the entire test run during the later evaluation of the video recordings with software, but only certain sections based on the flow depth. The final test setup is shown in the following figures.

Figure 3.4 - Overall test set-up (left), inlet and outlet construction with collecting net in the lower basin (center), inlet and outlet area in the model basin (right)

## 3.3 Experimental procedure

The experimental procedure can be divided into four phases. It starts with the preparation, which involves the general work before the actual experiments can begin. This includes attaching the camera to the ceiling, placing the measuring tapes along the edges of the basin, emptying the seeding net and aligning the spotlights. Depending on how soiled the basin was, it was also cleaned.

The first section of the experiment could then be started. The pump was operated until a water depth of 2 cm was reached in the basin. Once this water depth was reached, the pump was stopped and the seeding was distributed on the water surface. During this process, care was taken to ensure an even distribution of the particles. The pump was then started again. In the time it takes to reach the water depth of 3 cm required by the capillary limit, the current with the introduced seeding has enough time to develop over the entire basin. Once the water depth of 3 cm was reached, the recording was started. During the entire pumping operation, the increasing flow depth was tracked with the marking on the edge of the basin. As soon as it reached 9 cm, the intake was stopped, the pump switched off and the valve for the inflow closed.

After recording the inflow phase, a predefined time was waited before the outflow phase began in order to ensure that the model flow was as realistic as possible. According to Table 2.3, the time that passed in the prototype can be converted to the corresponding time in the model using the following formula:

$$t_M = t_P * \lambda^{-0,5} \text{ [s]} \quad (4)$$

Since pumped storage power plants are mainly peak load power plants, the diagram in Figure 3.5 was used to determine the approximate time that elapses between the end of pump operation and the start of turbine operation.

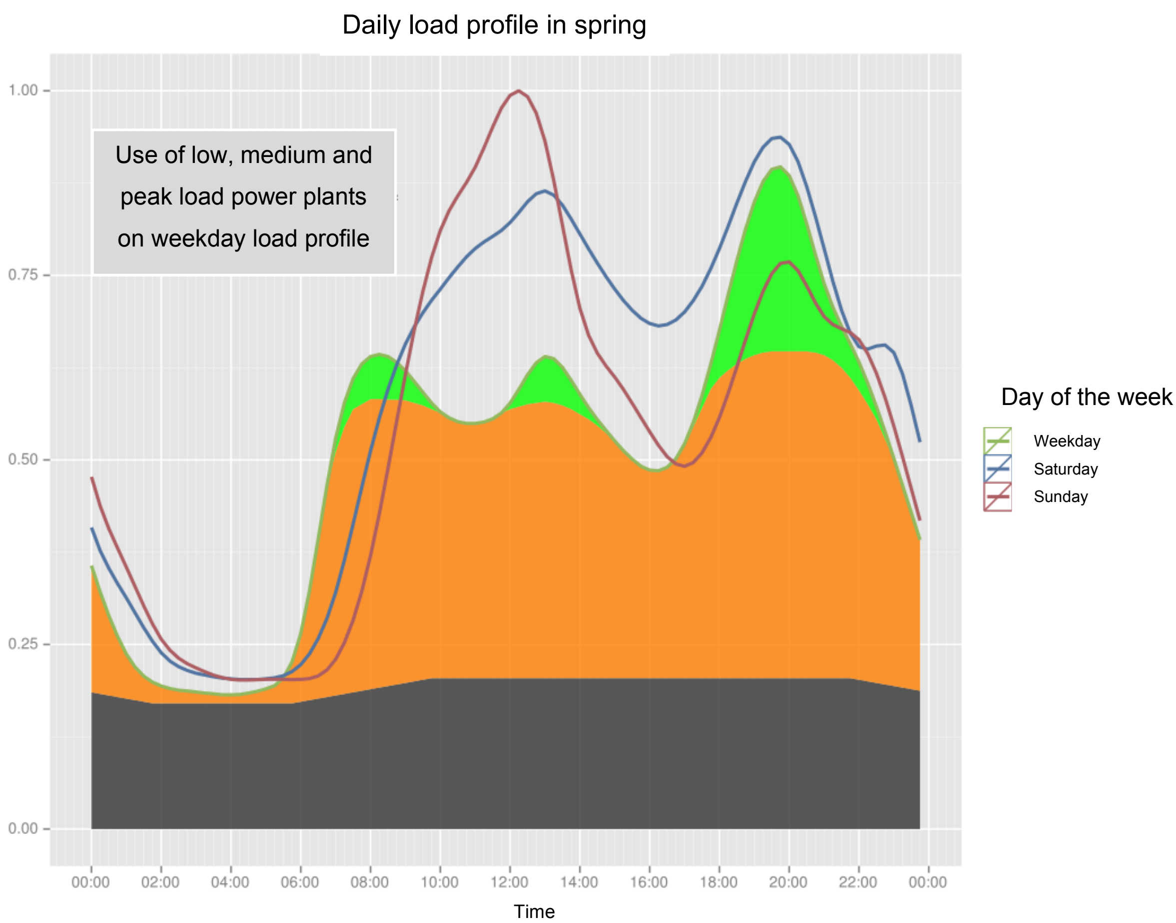


Figure 3.5 - Load profiles on different days and power plant use (adapted from Adam 2014)

The assumed end time of pump operation, the start time of turbine operation and the waiting times calculated and used for the model are listed in Table 3.11.

Table 3.11 - Selected and calculated waiting times in prototype and model

| End of pump operation | Start of turbine operation | Intermediate time prototype [minutes] | Intermediate time model [minutes] |
|---|---|---|---|
| 06:00 a.m. | 07:00 a.m. | 60 | ~ 4 |
| 06:00 a.m. | 12:00 p.m. | 360 | ~ 22 |
| 06:00 a.m. | 05:00 p.m. | 660 | ~ 40 |

Once the predetermined time had elapsed, the recording of the last part of the experiments could begin. To do this, the valve on the discharge pipe was opened and the recording was started. Similar to the recording of the inflow phase, the flow depth was also tracked during the outflow phase using the attached marking. The recording was stopped as soon as the water had fallen below the flow depth of 3 cm. Afterwards, it was waited until the basin had emptied completely. If necessary, the basin was cleaned of impurities before a new test run was started. The instructions for carrying out the experiment, which summarize this chapter on one page, can be found in the Appendix 1.9.

## 3.4 Analysis methods

The videos were analyzed using the open source software "Fudaa-LSPIV" already mentioned in chapter 2.2.2. The version of the software used was 1.7.0. The abbreviation LSPIV stands for "Large Scale Particle Image Velocimetry". This program was developed by Le Coz et al. (2014) and is used to analyse video and image files in order to detect and evaluate surface velocities and flow patterns. In this study, Fudaa-LSPIV was used for video processing, orthorectification, flow pattern calculation and result filtering.

The video processing was carried out in order to prepare the videos for the software and enable better evaluation. This also made it possible to reduce the amount of data and therefore minimize the computing time and storage space required. The measures carried out for each evaluation are summarized in the following table.

Table 3.12 - Video processing measures for improved evaluation in Fudaa-LSPIV

| **Measure** | **Inflow videos** | **Outflow videos** |
|---|---|---|
| Video segments | 3 Minutes | Full video |
| Frames per second | 5 FPS | 1 FPS |
| Resolution | 750 x 500 Pixels | 750 x 500 Pixels |

The purpose of orthorectification was to correct the distortion caused by the use of the camera's wide-angle lens. For this purpose, several reference points in the model basin were identified using the placed measuring tapes and read into the software. The software then generated a total of 900 to 1440 distortion-free images from the videos, depending on the video length and number of FPS, which are required for the PIV analysis.

The flow pattern calculation could then begin. The interrogation area (IA) and search area (SA) were defined for this purpose. The recommendations of Sutarto (2015), as described in chapter 2.2.2, were applied here. It turned out that an SA of 80 pixels is too large for the used video resolution, resulting in very long computing times without any improvement in the quality of the test results. For this reason, the optimum size for the SA was determined iteratively and independently from the recommendation in this study. The size of 25 pixels proved to be the most suitable for the SA. However, the size of the IA could be selected according to Sutarto and is 5 pixels larger than the SA in all four directions.

The grid points at which the software calculates the flow velocities and directions were also defined. Here, 60 grid points were arranged in the horizontal plane and 40 grid points in the vertical plane, so that a grid point was present every 5 cm in a model basin measuring 300 x 200 cm.

Finally, incorrect calculations were removed from the results obtained using the results filter provided by Fudaa-LSPIV. The procedure was as follows:

1) Perform flow pattern averaging for each image pair without filter to obtain a single flow pattern
2) Export flow velocities of all 2400 grid points to an Excel spreadsheet
3) Sort the table of velocities according to their magnitudes
4) Remove velocities outside the 1 - 99 % range
5) Enter the new highest and lowest velocities in Fudaa LSPIV velocity filter
6) Perform flow pattern averaging for each image pair with determined filter to obtain a single flow pattern

This procedure was determined and optimized iteratively through a large number of tests. The results of filtering in this way and the resulting images of the flow patterns are presented and discussed in chapter 4.2.

# 4 Results and Discussion

## 4.1 Experiment optimization

As described in chapter 3.2, numerous adjustments were made to the original experimental setup in order to optimize it for recording the flow structures in the model basin. These changes affected the seeding, the inflow and outflow as well as other components such as illumination and recording technology. The results of the tests to determine the optimum experimental setup and the reasons for the choice of the final setup are described in more detail in the following chapters.

### 4.1.1 Seeding

The main challenge in the test optimization was to find a seeding material that was suitable for surface PIV. A total of seven different seeding materials were examined, as already described in chapter 3.2. Due to the variety of seeding materials, different problems occured, which were to be eliminated using different measures. Table 4.1 summarizes the specific problems and solution approaches used for the individual materials.

Table 4.1 - Problems and applied solutions for different seeding materials

| Seeding | Problem | Solution approach |
|---|---|---|
| Charcoal (fine) | Particle size is too fine and cannot be removed from the water with available laboratory equipment | Avoid |
| Charcoal (coarse) | Particles sink to the bottom of the basin after a short retention time on the water surface | Increasing the density of the water by adding salt to it |
| | Water is completely saturated with salt before the particles remain floating on the water surface | Avoid |
| Crushed Walnutshells | Same problem as with Charcoal (coarse) | Avoid |
| Rice husk | Sinks if left in the water for a long time | Clean the model thoroughly after each experiment and use new material for the next experiment |
| | Tends to agglomerate slightly | Reduce surface tension with:<br>• Tensides (slight improvement)<br>• Ethanol (not implemented due to a lack of time) |
| Cork | Tends to agglomerate slightly | Reduce surface tension with:<br>• Tensides, ethanol (see above) |
| Polyethylene Beads | Tends to agglomerate slightly | Reduce surface tension with:<br>• Tensides, ethanol (see above) |
| Polystyrene Beads | Tends to agglomerate heavily; settles on the inlet or outlet structure and is not flushed out of the basin | Reduce surface tension with:<br>• Tensides, ethanol (see above)<br>• Color coating, see Albayrak and Lemmin (2021) (not implemented due to a lack of time) |

The table shows that the majority of the seeding materials tested were not suitable for surface PIV recordings despite the solutions applied. Due to unresolved or more prominent problems compared to other seeding materials, the following materials were avoided: charcoal (fine), charcoal (coarse), crushed walnutshells, rice husk and polystyrene beads.

The two remaining seeding materials, cork and polyethylene beads, showed very good characteristics for the test, although slight agglomeration also occurred with them. However, these had very little or no detectable effect on the evaluation by the PIV software. In analysis test runs of the test images, it was found that cork can be better detected and evaluated by the PIV software than polyethylene beads. For this reason, it was decided to use cork as seeding for the following experiments.

### 4.1.2 In- and Outflow

The description of the experiment in chapter 3.2 and the associated images show that no magnetic-inductive flow meter (MID) is integrated in the experimental setup. Therefore, the inflow of the pump and the outflow from the pipe were determined over time using a volume measurement. Furthermore, it was assumed that the inflow and outflow remained constant during the experiment.

The flow measurements showed an inflow in the model of approximately 0.3003 l/s ($Q_{Pump.}$) and an outflow of approximately 0.2625 l/s ($Q_{Turb.}$). It was especially noticeable that the outflow is strongly dependent on the water level in the basin. It is highest when the water level is 9 cm and decreases as the water level lowers. The flow values given here are mean values obtained from six measurement results in each case.

As the inflow and outflow no longer correspond to the value of 0.32 l/s used in chapter 3.1.3, these values were adjusted to the laboratory conditions. This adjustment results in the values for the model basin and the upscaled prototype, as shown in Table 4.2. These values were calculated in the same way as for the previous table, Table 3.6.

Table 4.2 - Adjusted dimensions of the model basin on a scale of 1:275 and scaled up

| Description | Abbreviation [Unit] | M 1:275 | Upscaled basin |
|---|---|---:|---:|
| Length | L [m] | 3.00 | 825 |
| Width | b [m] | 2.00 | 550 |
| Flow depth | h [m] | 0.09 | 24.75 |
| Storage volume | V [m³] | 0.54 | ~ 11,000,000 |
| Flow rate pump operation | $Q_{Pump.}$[l/s] | 0.3003 | 376,606 |
| Flow rate turbine operation | $Q_{Turb.}$[l/s] | 0.2625 | 329,201 |

Since the designed model basin and associated prototypes are already an upper basin of a pumped storage power plant, which do not exist in reality, but are still close to already existing ones, this adjustment does not limit the validity of the test results. Although the new flow rates are lower than the flow rates in the Goldisthal and Markersbach pumped storage power plants, they are still significantly higher than the flow rates of the Säckingen pumped storage power plant. This demonstrates that the new basin is still a realistic solution.

Due to the lower flow rates, it was necessary to verify the turbulence limit and the flow change limit again. The recalculation showed that the Reynolds number is 3200 and the flow is therefore in the turbulent range. The Froude number is 0.079 and is therefore at a sufficient distance from the critical value of one. These two model limits are therefore still fulfilled and the model remains valid. The detailed calculations can be found in the Appendix 1.10.

### 4.1.3 Other components

Initial recordings with the "Handycam HDR-CX520" camera from "Sony" showed that it has a too small field of view to capture the entire basin. This could have been solved by increasing the distance between the camera and the model basin. However, this distance is limited by the tripods provided and the height of the room. The tripod also proved to be disruptive during the recordings, as the tripod was visible on the video recordings and incorrect flow patterns occurred there during the PIV evaluation. For this reason, the "Hero 12" from "GoPro" was used and attached to the ceiling above the basin with a suction cup mount, which eliminated both of these problems.

Furthermore, the illumination from the fluorescent tubes directly above the basin proved to be problematic. These created large areas on the water surface that reflected the light so strongly that no seeding particles could be identified by the camera in these areas. This also led to incorrect flow patterns in the analysis of the recorded images. For this reason, two spotlights with two lamps each were used to illuminate the basin evenly without creating significant reflective water surfaces in the recordings.

At last, it was noticed that the seeding caused shadows on the sole of the basin due to the illumination method. These shadows were perceived as seeding by the PIV software. To avoid this error, the water in the model basin was colored white with a bath additive, which greatly reduced the formation of shadows at low water levels and completely prevented them at high water levels. With this procedure, the experimental setup was fully optimized for recording the flow patterns, which will be discussed in the following chapter.

## 4.2 Flow patterns

The optimized test setup made it possible to record and evaluate the flow patterns, with the relevant procedures already described in detail in chapters 3.3 and 3.4. This section will discuss the results obtained.

### 4.2.1 Inflow

The evaluation of the videos during the inflow process was carried out using three-minute video sections. These sections were selected using the marking visible in the video, which was used to track the water level within the basin.

Figure 4.1 shows the averaged flow pattern as the water level rose from 3 cm to 4 cm, describing the flow at the beginning of the inflow process. In contrast, Figure 4.2 shows the averaged flow pattern while the water level rose from 8 cm to 9 cm. This illustrates the flow at the end of the inflow process.

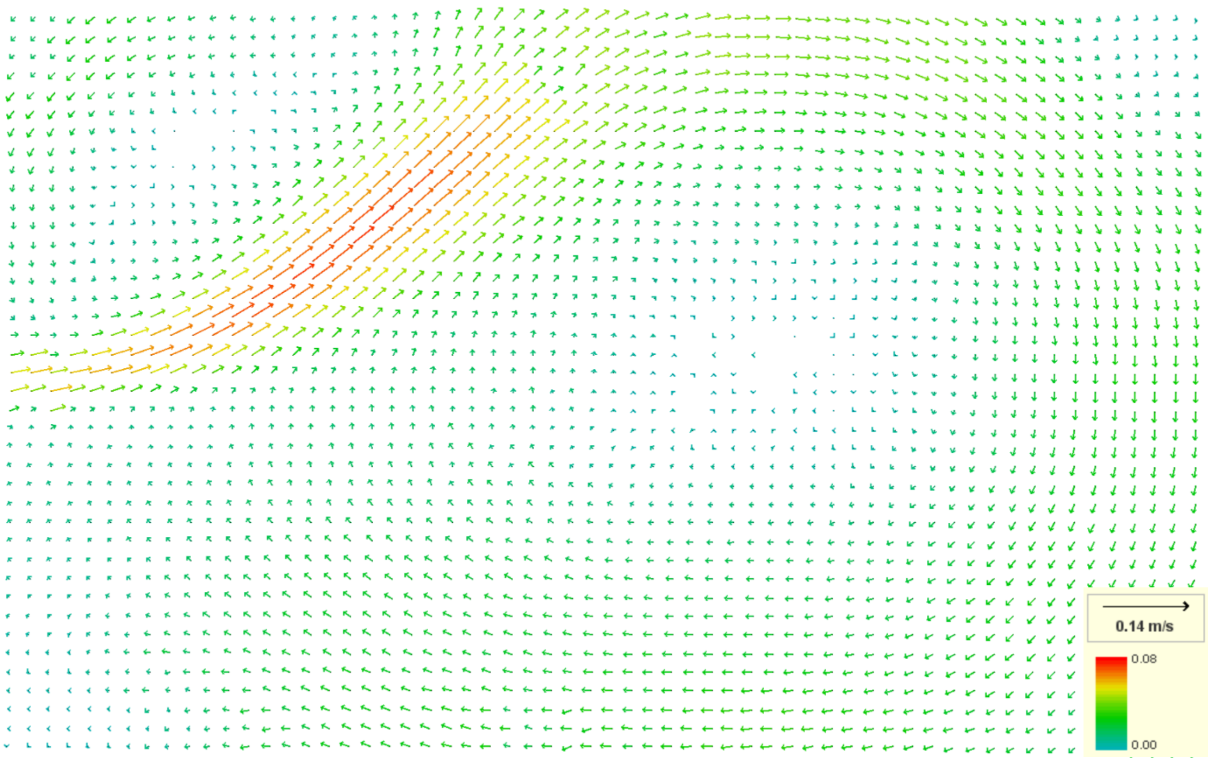


Figure 4.1 - Flow pattern in the model basin during inflow during a water level of 3 cm to 4 cm


Figure 4.2 - Flow pattern in the model basin during inflow during a water level of 8 cm to 9 cm

In both flow patterns, the inflow is deflected to the left immediately after entering the basin. The water flows towards the left wall of the basin and from there splits into two vortexes that flow through the basin. The smaller vortex in the top left-hand corner rotates anti-clockwise and continues this path until the water reaches the inlet and outlet area again and flows back into the basin from there. The larger vortex, which fills most of the basin, rotates clockwise until the water also reaches the inlet and outlet area and is directed back towards the center left side of the basin too. In the middle of the two vortexes, a zone is formed in which the flow velocities at the surface become very low.

The comparison of the two flow patterns shows that the flow velocities are greater at a low water level in the model basin than at a high water level. This is because the inlet and outlet structure is positioned at the sole of the basin and reaches a height of 5.50 cm. As a result, the surface flow is more influenced by the inflowing water when the water level is lower than the height of the inlet and outlet structure. If the water level is higher, this influence is less significant.

The lower flow velocity at higher water levels leads to an increase in the area within the two vortexes in which the flow velocity vectors are almost zero. This can be seen in the figures, as the area without a defined velocity in Figure 4.2 increases compared to Figure 4.1. At these points, the evaluation software cannot detect any changes between two pairs of images and therefore cannot determine any velocities. This could be resolved by further reducing the FPS. However, this led to inaccurate measurement results in the outer area of the vortexes. For this reason, this in-depth analysis was not carried out.

During the experiment, it was found that no visible movements could be seen with the bare eye in these zones. However, when the experiment recording is played back at high speed, minimal movements can be seen in the middle of the vortexes. These movements correspond to the vortex rotation currently being viewed, with the lowest surface speed in the center of the vortex.

An important aspect that is lost when averaging the flow velocities is the winding behavior of the flow. This is particularly dominant in the flow directed to the left directly after the water enters the basin. This phenomenon is clearly visible in Figure 4.3 . This representation was achieved by not averaging or filtering the PIV results. Therefore, this is not a representation of the flow over a period of three minutes, but a snapshot of the flow. This particular snapshot in Figure 4.3 shows the flow at the very beginning of the inflow process, while the water level is just over 3 cm.

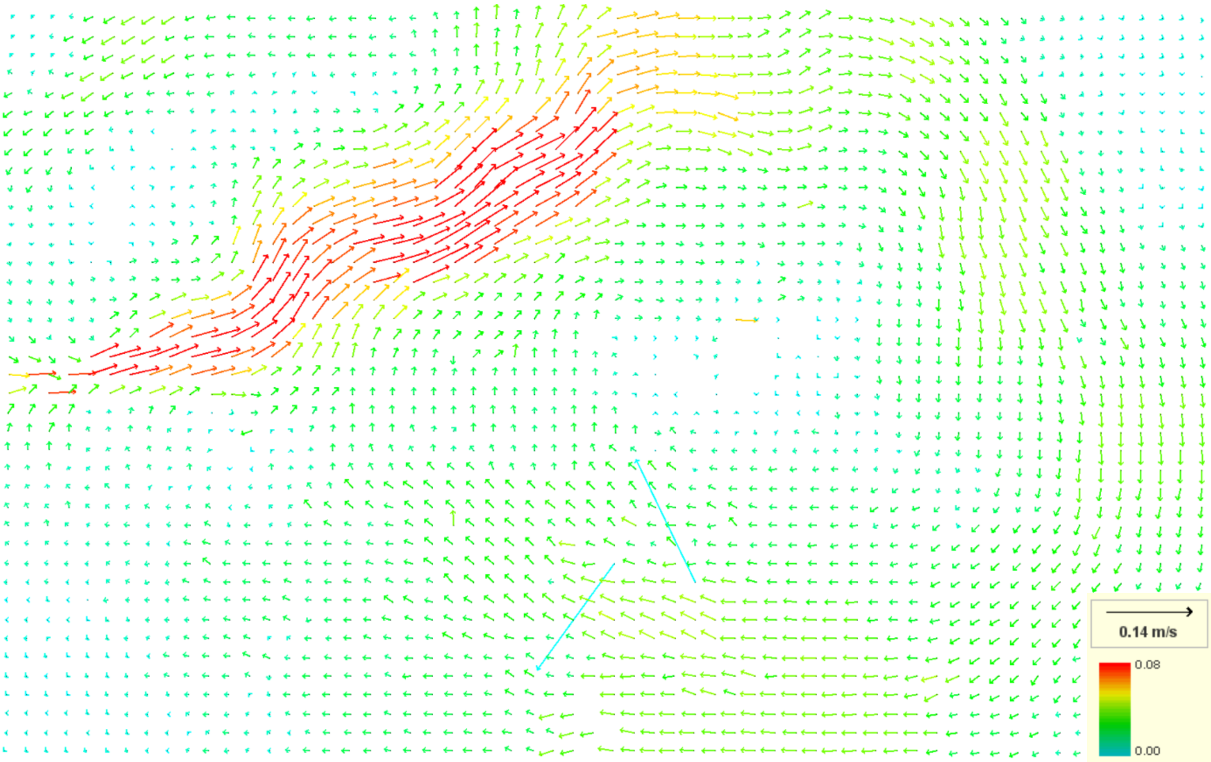


Figure 4.3 - Flow pattern in the model basin during inflow as a snapshot without velocity filter at a water level of approximately 3 cm

### 4.2.2 Outflow

In contrast to the inflow, the outflow was not evaluated in three-minute video segments, but the full length of the videos was used. This is due to the fact that the surface flow velocities during the outflow process are significantly lower. As a result, the software requires a lower number of frames per second (FPS) to detect changes between two image pairs. In order to continue to average a similar amount of flow data into an outflow pattern as for the inflow patterns, correspondingly longer video sections were required.

Three different types of outflow processes were recorded, which differ in the time span between the end of the inflow process and the start of the outflow process. This has already been explained in detail in chapter 3.3. Figure 4.4 shows the evaluation of the outflow process with a waiting time of four minutes without further result filtering, while Figure 4.5 shows the evaluation of the same test with result filtering.

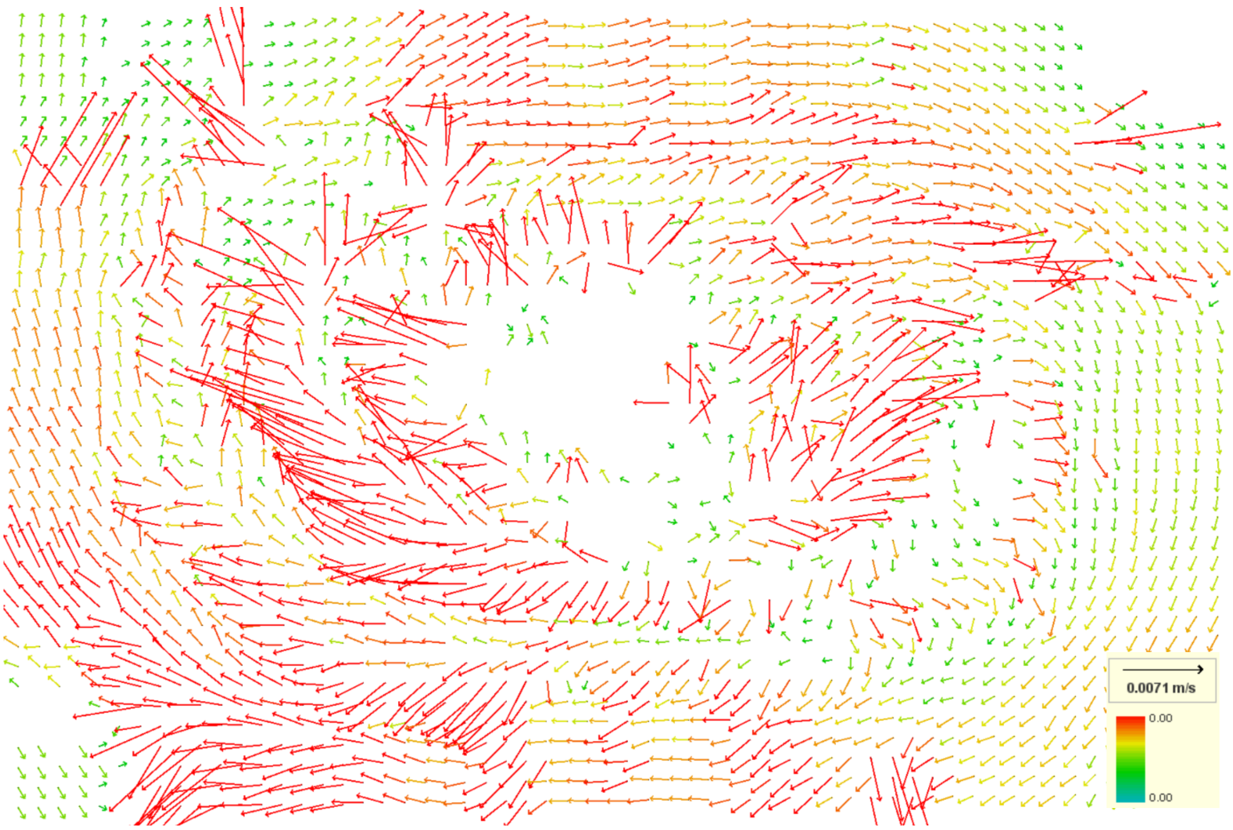


Figure 4.4 - Flow pattern in the model basin during outflow over the entire outflow duration without velocity filter

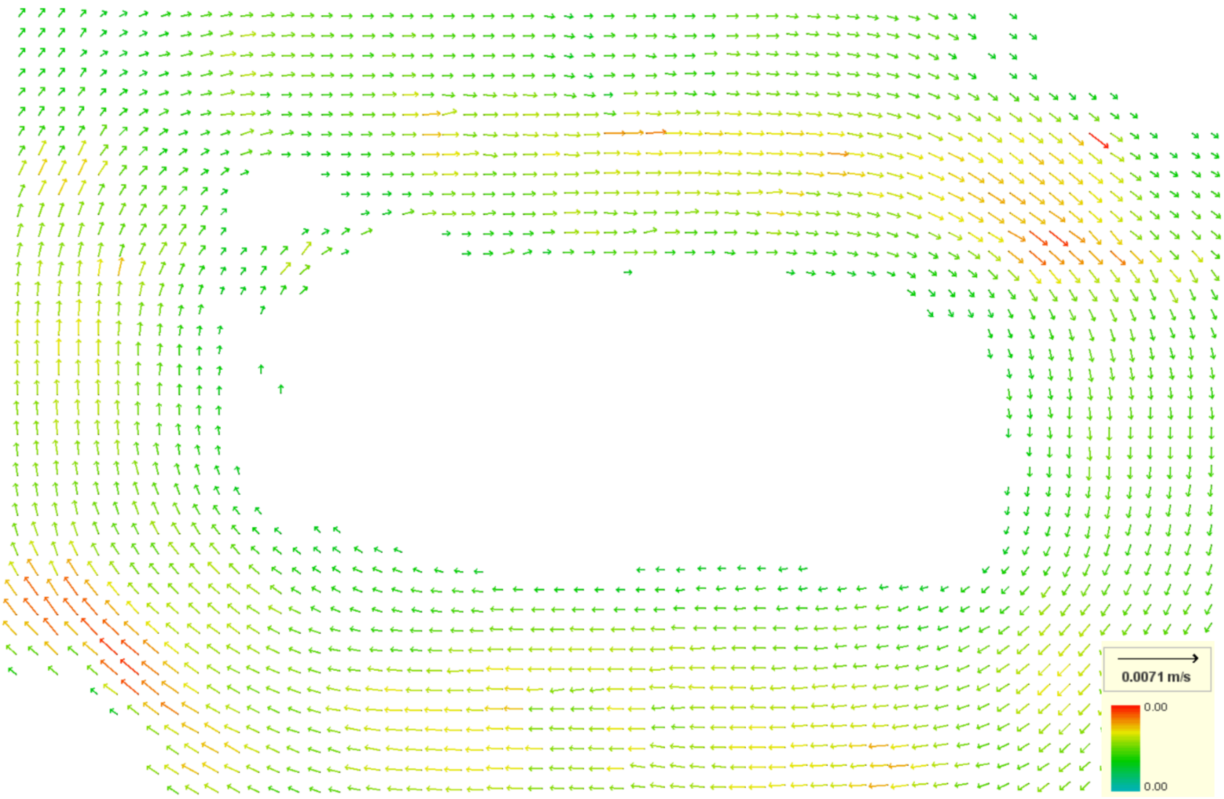


Figure 4.5 - Flow pattern in the model basin during outflow over the entire outflow duration with velocity filter

The comparison of these two flow patterns shows the importance and effectiveness of the velocity filter according to the method described in chapter 3.4. While the flow pattern in Figure 4.4 corresponds only slightly with the author's observations, Figure 4.5 shows a significantly higher similarity.

When looking at the filtered flow pattern, the circular flow that forms can be clearly seen. This flow fills the entire basin and rotates in a clockwise direction. This orientation of the flow suggests that when the influence of the inflowing water decreases, the larger vortex structure, which can be seen in Figure 4.1, dissolves the smaller vortex structure and then merges into the flow pattern that can be seen in Figure 4.5. In the center of this circular flow, similar to the flow patterns of the inflow process, no flow velocities can be detected with the software. However, if the video recordings are played back in fast-forward mode, circular flows that slow down towards the center can also be seen here.

It was observed that this clockwise rotating flow persists for the majority of the outflow process. Only in the last few minutes of the experiments does the rotation stop and the water moves evenly towards the inlet or outlet structure. The flow velocity is greater the closer the water is to this structure. As this specific flow pattern only makes up a small part of the test video, it cannot be seen in the analysis presented because of the averaging of the results.

This flow pattern becomes visible when the last few minutes of the test video are played in fast-forward. This flow pattern was also visible to the bare eye, which is why the author sketched the flows during the experiments. As a visualization using Fudaa-LSPIV could not be carried out successfully, Figure 4.6 shows the sketch illustrating the flow in the last minutes of the discharge process.

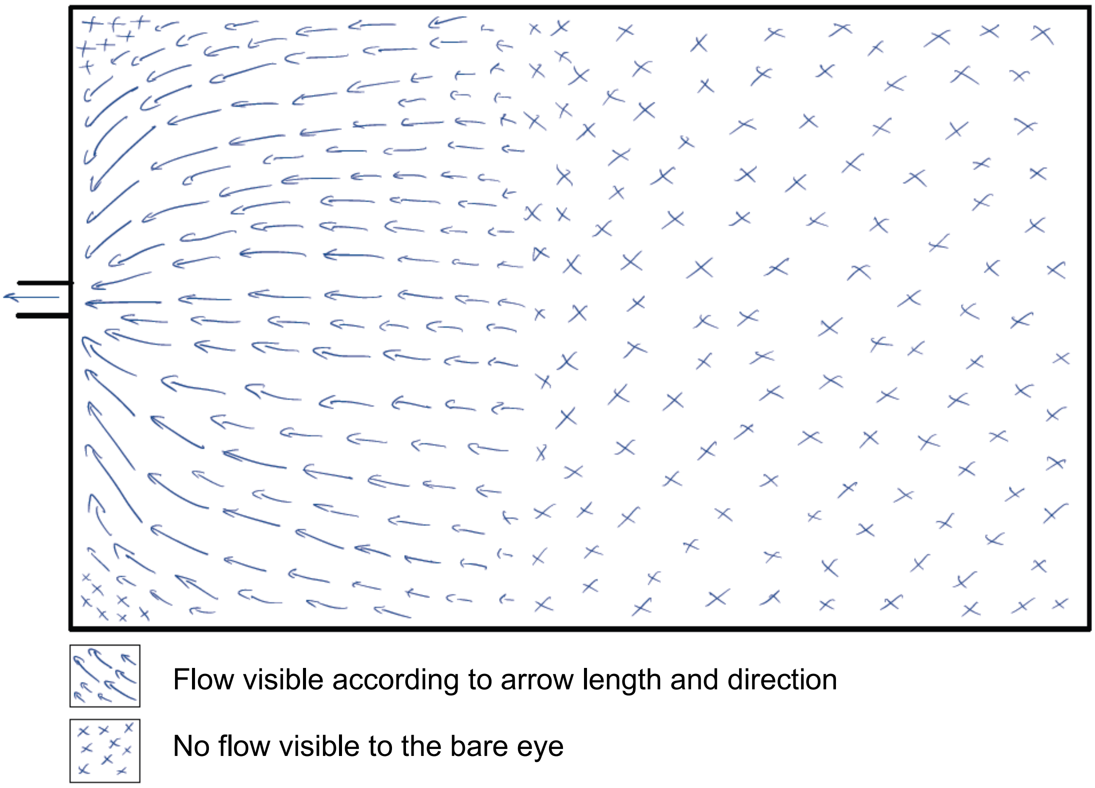


Figure 4.6 - Sketch of the flow in the last minutes of the outflow process

The experiments with waiting times of 22 minutes and 40 minutes are not described further in this paper. This is due to the fact that these flow patterns are very similar to the flow pattern of the experiment with the four-minute waiting time. In addition, the flow velocities were so low that it was not possible to generate descriptive flow patterns with Fudaa-LSPIV. Due to the limited processing time of this study, further analysis of these additional experiments was therefore not carried out.

## 4.3 Improvement approaches against sedimentation

The detailed presentation of the flow patterns in chapter 4.2 provides an improved perspective on the problem of sedimentation of upper basins by sediments carried in from the lower basin, as already described in chapter 2.1.2. This enables the formulation of solutions based on the findings of the flow patterns.

Sediment particles that enter the upper basin from the lower basin settle there due to the low flow velocities and the sometimes long retention times, as already described by Müller (2012). The areas in the upper basin with the lowest flow velocities are particularly at risk. During the inflow process, these areas can be seen in Figure 4.1 and Figure 4.2 as the centers of the vortex structures. During the outflow process, the entire center of the basin is at risk, as can be seen in Figure 4.5. In addition, the outflow process is particularly critical, as the flow velocities in the upper basin are significantly lower during this process compared to the inflow process.

The measures shown in Figure 2.3 can be used to reduce or prevent sedimentation in the upper basins. However, taking into account the results obtained in this study, a retroactive measure to avoid sedimentation, which has already been the subject of extensive research (Müller 2012; Müller et al. 2013a; Müller et al. 2013b), is of particular interest. This involves avoiding sedimentation in the upper basin by keeping the sediment particles in suspension for as long as possible. This can be achieved by increasing the turbulence in the basin. Measures for this could include reducing the waiting times between pumping and turbine operation or the targeted placement of vortex jets at favorable locations on the basin floor in order to prevent sedimentation, especially in vulnerable areas such as the middle of the basin.

Despite the possibility of reducing sedimentation described above, it also makes sense to take preventive measures to prevent sediment from entering the upper basin in advance. These measures offer the additional advantage that less sediment is passed through the turbines during turbine operation. Otherwise, depending on the composition of the sediment particles, hydroabrasion could occur on the turbine blades, as shown in Figure 2.2. However, this wear could be reduced by coating the turbine blades, for example with tungsten carbide, which increases resistance to wear. (cf. CeWOTec 2023).

# 5 Conclusion and Outlook

## 5.1 Conclusion

In this paper, the basics of pumped storage power plants and the sedimentation problem, Particle Image Velocimetry (PIV) and model tests were described. Based on this knowledge, several possible model basins were designed, of which the prototypes do not exist in reality, but are based on the dimensions of real upper basins. A final design of the basin was then constructed and the planned experiments were carried out. It was found that numerous optimization measures were required before the experiments could be recorded in such a way that the flow patterns could be visualized using analysis software. After implementing several optimization measures, it was possible to create the test videos as needed. The Fudaa-LSPIV software was then used to generate the flow patterns that can be viewed in chapter 4.2. With these flow patterns, it is possible to create numerical flow simulations in order to investigate the sedimentation problem of upper basins of pumped storage power plants as well as possible solutions against sedimentation, some of which have already been addressed in chapter 4.3.

With the information acquired from this study, the research questions formulated at the beginning can be answered as follows:

- Why do sediment deposits occur in pumped storage basins?

  In upper basins of pumped storage power plants with natural inflow, sediment deposition occurs due to the imbalance between sediment input and output. This imbalance is caused by the difference in density between the inflowing sediment-rich water and the low-sediment water in the basin. The sediment is transported to the lowest point of the basin and settles there.

  In all types of upper basins, whether with or without a natural inlet, sedimentation occurs due to sediment input from the lower basin. These lower basins usually have a natural inflow and therefore sediment input as described in the previous paragraph. During pumping operation, the sediment, consisting mainly of suspended particles, is transported to the upper basin, where it settles due to low flow velocities and long retention times.

- What is Particle Image Velocimetry (PIV) and how can it be used to capture flow patterns in the model?

Particle Image Velocimetry (PIV) is a method for the large-scale detection of velocities in a liquid or gaseous medium. For this purpose, a tracer material is introduced into the medium, which tracks the movements of it. These movements are captured by a camera with according illumination and an evaluation software can determine the direction and speed of the movement of particles in the medium by comparing two images of this recording in immediate succession. By determining this data over a large area, flow patterns can be calculated and displayed.

- What do the flow patterns in an upper basin look like in the model during turbine or pump operation?

The experiments conducted show that during pump operation (inflow process), two vortex structures of different sizes are formed that rotate in opposite directions. The inflowing water is deflected to the left. As the water level in the basin rises, the surface flow velocities decrease. In turbine operation (discharge process), the flow velocities are significantly lower and only a clockwise rotating vortex is formed. This vortex dissolves at the end of the discharge process and the water flows evenly to the inlet or outlet structure. In general, there is a reduction in the surface flow velocity as the water level rises, inside the vortex structures and during turbine operation.

## 5.2 Outlook

This study is part of an extensive project dealing with the sedimentation of upper basins of pumped storage power plants. Therefore, tasks such as the creation of numerical models incorporating the knowledge gained here, the implementation and application of solution measures in the numerical model and field tests to verify the tested measures in practice follow on from this study.

Apart from the extent of this project, additional steps should be taken to extend the quality and quantity of the research results of this study. One possible improvement could be to optimize the seeding material used to reduce agglomeration. In addition, the flow velocities in the water body itself, especially at the bed of the basin, are of interest. This would require PIV images using a laser sheet.

These additional investigations will make it possible to develop solutions to counteract the sedimentation of reservoirs, including the upper basins of pumped storage power plants, which is being accelerated by climate change, and therefore contribute to the expansion of the sustainable energy production.

# List of References

Abdulwahab, M.R., Ali, Y., Habeeb, F., Borhana, A., Abdelrhman, A.M., Al-Obaidi, S.M.A. (2022): „*A Review in Particle Image Velocimetry Tecniques (Developments and Applications)*“. In: *Journal of Advanced Research in Fluid Mechanics and Thermal Sciences*. Penerbit Akademia Baru (65).

Adam, K. (2014): „*Spitzenlast*“. *Wikipedia*.

Albayrak, I., Lemmin, U. (2021): „*Large scale PIV-measurements on the water surface of turbulent open-channel flow*“. In: Grenoble, France.

Auel, C. (2023): „*Maßstabseffekte*“(Lecture script). Muenster, Germany.

Bundesregierung (2023): „*Anteil der Erneuerbaren Energien steigt weiter*“. *Die Bundesregierung*. Accessed 08.11.2023 from https://www.bundesregierung.de/breg-de/schwerpunkte/klimaschutz/faq-energiewende-2067498#:~:text=2021%20lag%20der%20Anteil%20der,weiter%20auf%20rund%2052%20Prozent.

CeWOTec (2023): „*Wolframcarbid-Beschichtung*“. Accessed 06.01.2024 from https://www.cewotec.de/beschichtung/wolframcarbid-beschichtung/.

Clauss Ingenieure (o. J.): „*Pumpspeicherwerk Goldisthal - 1.060-MW-Kavernenkraftwerk*“. *Clauss Ingenieure*. Accessed 12.01.2023 from http://www1.clauss-ingenieure.de/pumpspeicherwerk-goldisthal/.

DWA (2006): „*Entlandung von Stauräumen*“. Hennef, DWA.

Giesecke, J., Heimerl, S., Mosonyi, E. (2014): „*Wasserkraftanlagen - Planung, Bau und Betrieb*“. 6. Aufl. Berlin, Germany: Springer Vieweg.

Google LLC (2022): „*Google Earth*“. Google LLC.

Heller, V. (2011): „*Scale effects in physical hydraulic engineering models*“. In: *Journal of Hydraulic Research*. (49), S. 293–306.

Jenzer Althaus, J., De Cesare, G., Schleiss, A. (2008): „*Abführung von Feinsedimenten über Triebwassersysteme als nachhaltige Maßnahme gegen Stauraumverlandung*“. In: *Neue Anforderungen an den Wasserbau*. Zurich, Switzerland: Laboratory of Hydraulic Engineering Hydrology and Glaciology of the ETH Zurich S. 349–360.

Kantoush, S.A., Schleiss, A.J. (2009): „*Large-Scale PIV Surface Flow Measurements in Shallow Basins with Different Geometries*“. In: *Journal of Visualisation*. Springer (12), S. 361–373.

Komori (小森) (2023): „Technical drawing of the final experimental setup *(京都大学実験槽工事)*“. Kyoto University, Kyoto, Japan.

Le Coz, J., Jodeau, M., Hauet, A., Marchard, B., Le Boursicaud, R. (2014): „*Image-based velocity and discharge measurements in field and laboratory river engineering studies using the free FUDAA-LSPIV software*“. Lausanne, Switzerland: EDF.

Martin, H., Pohl, R. (Hrsg.) (2000): „*Technische Hydromechanik Band 4 - Hydraulische und numerische Modelle*“. 1. Edition Dresden, Germany: Verlag Bauwesen.

Mohringer, T. (2022): „*Ein-/ Auslaufbauwerke großer Pumpspeicherkraftwerke*". (Project poster) Karlsruhe: Institute for Water and River Development.

Mohringer, T. (2012): „*Entwurf von Ein- und Auslaufbauwerken von Pumpspeicherwerken*". Karlsruhe, Germany: Karlsruhe Institute of Technology (KIT).

Müller, M. (2012): „*Influence of in- and outflow sequences on flow patterns and suspended sediment behavior in reservoirs*". Lausanne, Switzerland: École Polytechnique Fédérale de Lausanne.

Müller, M., De Cesare, G., Schleiss, A. (2013a): „*Einfluss von Pumpspeichersequenzen auf die Strömungsverhältnisse und das Absetzverhalten von Feinsedimenten in Stauseen*". In: *Wasser Energie Luft*. Baden, Switzerland.

Müller, M., Schleiss, A., De Cesare, G. (2013b): „*Influence of pumped-storage operation on reservoir sedimentation*". In: *Changing times: infrastructure development to infrastructure management*. Seattle, USA S. 1823–1834.

Ortmanns, C. (2006): „*Entsander von Wasserkraftanlagen*". Zurich, Switzerland: ETH Zürich.

Patalano, A., Garcia, C.M., Rodriguez, A. (2017): „*Rectification of Image Velocity Results (RIVeR): A simple an user-friendly toolbox for large scale water surface Particle Image Velocimetry (PIV) and Particle Tracking Velocimetry (PTV)*". In: *Computers & Geosciences*. Cordoba, Argentinia: Elsevier.

Raffel, M., Willert, C.E., Scarano, F., Kähler, C.J., Wereley, S.T., Kompenhans, J. (2018): „*Particle Image Velocimetry*" *- A Practical Guide*. 3. Edition Springer Cham.

Schleiss, A., De Cesare, G., Althaus, J.J. (2010): „*Verlandung von Stauseen gefährdet die nachhaltige Nutzung der Wasserkraft*". In: *Wasser Energie Luft*. Baden, Switzerland (102), S. 31–40.

Schleiss, A., Oehy, C. (2002): „*Verladung von Stauseen und Nachhaltigkeit*". In: *Wasser Energie Luft*. 94 (7–8), doi: http://doi.org/10.5169/seals-939647.

Schluchseewerk AG (2023): „*Das Kavernenkraftwerk Säckingen - große Leistung tief im Berg*". *Schluchseewerk AG*. Accessed 12.11.2023 from https://www.schluchseewerk.de/wo-wir-sind/hotzenwaldgruppe/eggbergbecken.

Schlurmann, O. (2002): „*Wasserbauliches Versuchswesen*". Bergische Universität Wuppertal.

Schütz, P. (2019): „*Das Eggbergbecken wird saniert und bietet ohne Wasser einen komplett anderen Blick*". *Südkurier*. Accessed 12.11.2023 from https://www.suedkurier.de/region/hochrhein/rickenbach/Das-Eggbergbecken-wird-saniert-und-bietet-ohne-Wasser-einen-komplett-anderen-Blick;art372616,10150790.

Strobl, T., Zunic, F. (2006): „*Wasserbau*". Munich, Germany: Springer Berlin Heidelberg.

Sutarto, T.E. (2015): „*Application of large scale particle image velocimetry (LSPIV) to identify flow pattern in a channel*". In: *Procedia Engineering*. Samarinda, Indonesia: Elsevier Ltd. S. 213–219.

Vattenfall GmbH (2023a): „*Pumpspeicherkraftwerk Goldisthal - das größte Pumpspeicherkraftwerk Deutschlands*". *VATTENFALL*. Accessed 29.11.2023 from https://powerplants.vattenfall.com/de/goldisthal/.

Vattenfall GmbH (2023b): „*Pumpspeicherwerk Markersbach - eines der größten Wasserkraftwerke Europas*“. *VATTENFALL*. Accessed 29.11.2023 from https://powerplants.vattenfall.com/de/markersbach/.

VDE Kassel (2006): „*Exkursion in das Pumpspeicherwerk Goldisthal / Thüriger Wald*“. (Exkursionsbericht) Kassel, Germany: VDE Kassel.

Voss-de Haan, P. (2000): „*Laser*“. In: *Lexikon der Physik*. Heidelberg: Spektrum Akademischer Verlag.

Vreugdenhil, C.B. (1994): „*Shallow-water flows*“. In: *Numerical Methods for Shallow-Water Flow*. Dordrecht, Netherlands: Springer, Dordrecht (Water Science and Technology Library).

# Appendix

## 1.1 Rules of thumb

Appendix 1 - Limiting criteria to avoid significant scale effects in various hydraulic flow phenomena (Heller 2011)

| Investigation | Phenomenon | Rule of thumb | Related prototype features | Reference |
|---|---|---|---|---|
| Air-entraining free vortex at horizontal intake | Flow conditions | $Q_i/(z_i\nu) > 30{,}000$ and $\rho Q_i^2 z_i/(A_i^2\sigma) > 10{,}000$ | Scale series: largest discharge 0.009 $m^3/s$, largest submergence depth 0.8 m, constant intake diameter = 0.0762 m | Anwar *et al.* (1978) |
| Broad-crested weir | Discharge coefficient | Overfall height ≥ 0.07 m | Weir length 0.15 – 5 m, weir width 4.88 m | Hager (1994) |
| Dam break wave | Sudden failure, dam in smooth rectangular channel | Still water depth ≥ 0.30 m | n.a. | Lauber and Hager (1998) |
| Dam with ski jump | Lateral overfall weir, spillway capacity, ski jump, flow conditions in stilling basin | Scale 1 : 30 | Upper Siebertalsperre, dam height 90 m, $Q_d = 140$ $m^3/s$ | Bretschneider, in Kobus (1980) |
| Dike breaching | Hydraulics over dike consisting of uniform and non-cohesive material | Unit discharge ≥ 20 1/s and $d_g \geq$ 1 mm | Scale series: largest scale with dike height = width = 0.40 m and $d_g$ = 8 mm | Schmocker and Hager (2009) |
| Hydraulic jump | Sequent depths ratio $h_2/h_1$ | $V_1h_1/\nu > 100{,}000$ for $\mathsf{F}_1 < 10$ and $h_1/b$ <0.1 | Scale series: maximum $h_1 = 0.063$ m, maximum $\mathsf{F}_1 = 42.7$ | Hager and Bremen (1989) |
| Hydraulic jump | Void fraction and bubble count rate distributions, bubble chord time | $\rho V_1 h_1/\mu > 100{,}000$ | Scale series: maximum $h_1 = 0.024$ m, maximum $b$ =0.50 m, maximum $\mathsf{F}_1 = 8.5$ | Chanson (2009) |
| Impulse wave | Generation by subaerial landslide | $\mathsf{R}_I \geq 300{,}000$ and $\mathsf{W}_I \geq 5000$ resulting in $h \geq 0.200$ m | Scale series: maximum $h = 0.60$ m, $1.7 \geq V_s/(gh)^{1/2} \leq 4.3$ | Heller *et al.* (2008) |
| Mountain river | Bed morphology | Scale 1 : 10 to 1 : 20 | Steinibach, $d_m = 0.20$ m, $d_{90} = 0.52$ m, $d_{max} = 0.90$ m, slope 3 – 13% | Weichert (2006) |
| River expansion | Bed load transport | Scale 1 : 55, $d_g$ >0.22 mm and correction grain size distribution | $d_m = 0.043$ m, $d_{90} = 0.096$ m | Zarn (1992) |
| Rubble mound breakwater | Stability | Limiting scale as a function of prototype wave height in Fig. 1 of Oumeraci (1984) | Prototype wave height up to 13 m | Oumeraci (1984) |
| Scour | Bridge pier and abutment scour depth development prediction with Eq. (1) of Oliveto and Hager (2005) | 0.60 < threshold Froude number < 1.20, width pier/$b$ ≥ 0.05, width abutment/$b$ ≥0.05 | Model tests: width pier = 0.022 – 0.500 m, width abutment = 0.05 – 0.20 m, 0.45 ≤ $t$≤ 21.0 days, $b$ = 1.0 m, 0.03 ≤$h$ ≤ 0.18 m, $d_{50} \geq 0.80$ mm, $1.07 \leq V/(g'd_{50})^{1/2} < 4.26$ with $g' = [(\rho_s - \rho)/\rho]g$ | Oliveto and Hager (2005) |
| Scour | Effect of large-scale turbulence on equilibrium scour depth at cylinders | Cylinder diameter > 0.400 m for scale effect ≤ 5% | Model tests: cylinder diameter = 0.064 – 0.406 m, average velocity = 0.46 m/s, $v^*/v^*_c = 0.80$, $d_m = 1.05$ mm, $h$ =1.000 m | Ettema *et al.* (2006) |
| Sharp-crested weir | Lower nappe profile | Overfall height ≥ 0.045 m | Scale series: maximum overfall height = 0.045 m | Ghetti and D'Alpaos (1977) |
| Ski jump | Jet throw distance | Approach flow depth ≥ 0.04 m | Scale series: largest water depth 0.07 m | Heller *et al.* (2005) |
| Skimming flow on stepped spillway | Turbulence level, entrained bubble sizes and interfacial areas | $\rho(gh_c^3)^{1/2}/\mu > 500{,}000$ and step height > 0.02 m | Scale series: maximum step height 0.143 m, spillway slopes 3.4 – 50° | Chanson (2009) |
| Spillway | Amount of air entrainment from aerator | $V/[\sigma/(\rho h)]^{1/2} > 110$ | Measurements in models and a small prototype and consideration of further prototype data | Rutschmann (1988) |
| Stepped spillway | Flow velocity profile air–water mixture | Scale ≥ 1 : 15 | Step height 0.6 m, maximum specific discharge 20 $m^2/s$ | Boes (2000) |
| Surf zone beach profile | Volume of transported sand | Scale ≥ 1 : 7.5, $d_{50} = 0.13$ mm, significant wave height 0.20 m, peak wave period 2.0 s | $d_{50} = 0.335$ mm, significant wave height 1.5 m, peak wave period 6.0 s | Ranieri (2007) |
| Vertical plunging circular jet | Void fraction and bubble count rate distributions, bubble size | $\rho V_j^2 d_j/\sigma > 1000$ | Scale series: largest jet diameter 0.025 m, jet Froude number up to 10 | Chanson (2009) |
| Wave overtopping at coastal structures | Overtopping velocity | $2(R - R_c)^2/(\nu T) > 1000$ and $V_R^2 h_R \rho/\sigma > 10$ | Theoretically deduced | Schüttrumpf and Oumeraci (2005) |
| Wave run-up | Run-up velocity | $2(R - R_c)^2/(\nu T) > 1000$ and $V_R^2 h_R \rho/\sigma > 10$ | Theoretically deduced | Schüttrumpf and Oumeraci (2005) |
| Water wave | Force on slope during wave breaking | Wave height > 0.50 m | Scale series: maximum wave height 1.25 m | Skladnev and Popov (1969) |
| Water wave | Theoretical effect of surface tension | $T > 0.35$ s, $h > 0.02$ m | Wave with wave length where surface tension effects contribute less than 1% | Hughes (1993) |

Notes: n.a.=not available; for symbols, see Notation.

Appendix 2 - Typical model scales as compromise between reasonable size (economics) and moderate scale effects; scale effects may therefore not necessarily be negligible (Heller 2011)

| Investigation | Typical scale | Reference |
|---|---|---|
| Beach, shoreline process | 1 : 100 (vertical), 1 : 300 (horizontal) | Le Méhauté (1990) |
| Bottom outlet | 1 : 50 to 1 : 100 | Le Méhauté (1990) |
| Breakwater stability in short waves | 1 : 30 to 1 : 50 | Le Méhauté (1990), Hughes (1993) |
| Force on solid body in short waves | 1 : 10 to 1 : 50 | Hughes (1993) |
| Harbour penetration of short waves | 1 : 50 to 1 : 150 | Hughes (1993) |
| Hydraulic model to investigate cavitation | 1 : 10 to 1 : 30 | Keller, in Kobus (1980) |
| Intake | 1 : 50 to 1 : 100 | Le Méhauté (1990) |
| Long waves in distorted estuarine system | 1 : 100 to 1 : 150 (vertical), 1 : 300 to 1 : 800 (horizontal) | Hughes (1993) |
| Long waves in distorted harbour or port | 1 : 50 to 1 : 100 (vertical), 1 : 80 to 1 : 400 (horizontal) | Hughes (1993) |
| Long waves in undistorted harbour | 1 : 50 to 1 : 150 | Hughes (1993) |
| Long waves in undistorted inlet | 1 : 75 to 1 : 150 | Hughes (1993) |
| Offshore and harbour investigation (diffraction, refraction, reflection) | 1 : 60 to 1 : 150 | Kohlhase and Dette, in Kobus (1980) |
| River | 1 : 100 (vertical), 1 : 800 (horizontal) | Le Méhauté (1990) |
| Rockfill cofferdam | 1 : 30 to 1 : 50 | Le Méhauté (1990) |
| Rubble mound breakwater stability | 1 : 20 to 1 : 80 | Oumeraci (1984) |
| Ship dynamics problem | 1 : 100 | Le Méhauté (1990) |
| Ship motion study in long waves | 1 : 80 to 1 : 120 | Hughes (1993) |
| Short wave reflection at porous breakwater | 1 : 10 to 1 : 20 | Oumeraci (1984) |
| Spillway | 1 : 50 to 1 : 100 | Le Méhauté (1990) |
| Stability study in waves (rubble mound breakwater, for input to compression study) | 1 : 5 to 1 : 30 | Kohlhase and Dette, in Kobus (1980) |
| Water power structure | 1 : 50 to 1 : 100 | Le Méhauté (1990) |
| Waves on structure (reflection, wave pressure distribution) | 1 : 30 to 1 : 60 | Kohlhase and Dette, in Kobus (1980) |
| 2D wave transformation of short waves | 1 : 10 to 1 : 50 | Hughes (1993) |
| 3D wave transformation of short waves | 1 : 25 to 1 : 75 | Hughes (1993) |

## 1.2 Calculation Eggbergbasin

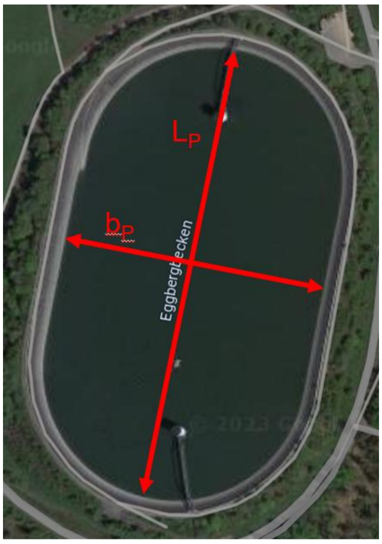


Appendix 3 - Satellite image of the upper basin of the Säckingen pumped storage power plant operated by Schluchseewerk AG (Google LLC 2022)

Appendix 4 - Properties of the upper basin of the Säckingen pumped storage power plant

| Description | Abbreviation [Unit] | Value |
|---|---|---|
| Length | $L_P$ [m] | 490 |
| Width | $b_P$ [m] | 300 |
| Flow depth | $h_P$ [m] | 14.29 |
| Storage volume | $V_P$ [m³] | ~ 2,100,000 |
| Flow rate pump operation | $Q_{P.,Pump.}$ [l/s] | 67,000 |
| Flow rate turbine operation | $Q_{P.,Turb.}$ [l/s] | 96,000 |

Appendix 5 - Scaling of the upper basin of the Säckingen pumped storage power plant according to Froude's law of similarity

| Scale M [-] | Length $L_M$ [m] | Width $b_M$ [m] | Flow depth $h_M$ [m] | Flow rate pump operation $Q_{M.,Pump.}$ [l/s] | Flow rate turbine operation $Q_{M.,Turb.}$ [l/s] |
|---|---|---|---|---|---|
| 1:50 | 9.80 | 6.00 | 0.29 | 3.79 | 5.43 |
| 1:75 | 6.53 | 4.00 | 0.19 | 1.38 | 1.97 |
| 1:100 | 4.90 | 3.00 | 0.14 | 0.67 | 0.96 |
| 1:150 | 3.27 | 2.00 | 0.10 | 0.24 | 0.35 |
| 1:175 | 2.80 | 1.71 | 0.08 | 0.17 | 0.24 |
| 1:200 | 2.45 | 1.50 | 0.07 | 0.12 | 0.17 |
| 1:250 | 1.96 | 1.20 | 0.06 | 0.07 | 0.10 |
| 1:275 | 1.78 | 1.09 | 0.05 | 0.05 | 0.08 |

Appendix 6 - Scaling of the upper basin of the Säckingen pumped storage power plant according to Reynold's law of similarity

| Scale M [-] | Length $L_M$ [m] | Width $b_M$ [m] | Flow depth $h_M$ [m] | Flow rate pump operation $Q_{M.,Pump.}$ [l/s] | Flow rate turbine operation $Q_{M.,Turb.}$ [l/s] |
|---|---|---|---|---|---|
| 1:50 | 9.80 | 6.00 | 0.29 | 1340 | 1920 |
| 1:75 | 6.53 | 4.00 | 0.19 | 893 | 1280 |
| 1:100 | 4.90 | 3.00 | 0.14 | 670 | 960 |
| 1:150 | 3.27 | 2.00 | 0.10 | 447 | 640 |
| 1:175 | 2.80 | 1.71 | 0.08 | 383 | 549 |
| 1:200 | 2.45 | 1.50 | 0.07 | 335 | 480 |
| 1:250 | 1.96 | 1.20 | 0.06 | 268 | 384 |
| 1:275 | 1.78 | 1.09 | 0.05 | 244 | 349 |

## 1.3 Calculation Markersbachbasin


Appendix 7 - Satellite image of the upper basin of Vattenfall AG's Markersbach pumped storage power plant (Google LLC 2022)

Appendix 8 - Properties of the upper basin of the Markersbach pumped storage power plant

| **Description** | **Abbreviation [Unit]** | **Value** |
|---|---|---|
| Length | $L_P$ [m] | 990 |
| Width | $b_P$ [m] | 450 |
| Flow depth | $h_P$ [m] | 13.47 |
| Storage volume | $V_P$ [m³] | ~ 6,000,000 |
| Flow rate pump operation | $Q_{P.,Pump.}$ [l/s] | No information |
| Flow rate turbine operation | $Q_{P.,Turb.}$ [l/s] | 420,000 |

Appendix 9 - Scaling of the upper basin of the Markersbach pumped storage power plant according to Froude's law of similarity

| **Scale** M [-] | **Length** $L_M$ [m] | **Width** $b_M$ [m] | **Flow depth** $h_M$ [m] | **Flow rate pump operation** $Q_{M.,Pump.}$ [l/s] | **Flow rate turbine operation** $Q_{M.,Turb.}$ [l/s] |
|---|---|---|---|---|---|
| 1:50 | 19.80 | 9.00 | 0.27 | - | 23.76 |
| 1:75 | 13.20 | 6.00 | 0.18 | - | 8.62 |
| 1:100 | 9.90 | 4.50 | 0.13 | - | 4.20 |
| 1:150 | 6.60 | 3.00 | 0.09 | - | 1.52 |
| 1:175 | 5.66 | 2.57 | 0.08 | - | 1.04 |
| 1:200 | 4.95 | 2.25 | 0.07 | - | 0.74 |
| 1:250 | 3.96 | 1.80 | 0.05 | - | 0.43 |
| 1:275 | 3.60 | 1.64 | 0.05 | - | 0.33 |

Appendix 10 - Scaling of the upper basin of the Markersbach pumped storage power plant according to Reynold's law of similarity

| **Scale** M [-] | **Length** $L_M$ [m] | **Width** $b_M$ [m] | **Flow depth** $h_M$ [m] | **Flow rate pump operation** $Q_{M.,Pump.}$ [l/s] | **Flow rate turbine operation** $Q_{M.,Turb.}$ [l/s] |
|---|---|---|---|---|---|
| 1:50 | 19.80 | 9.00 | 0.27 | - | 8400 |
| 1:75 | 13.20 | 6.00 | 0.18 | - | 5600 |
| 1:100 | 9.90 | 4.50 | 0.13 | - | 4200 |
| 1:150 | 6.60 | 3.00 | 0.09 | - | 2800 |
| 1:175 | 5.66 | 2.57 | 0.08 | - | 2400 |
| 1:200 | 4.95 | 2.25 | 0.07 | - | 2100 |
| 1:250 | 3.96 | 1.80 | 0.05 | - | 1680 |
| 1:275 | 3.60 | 1.64 | 0.05 | - | 1527 |

## 1.4 Sketches of the basins

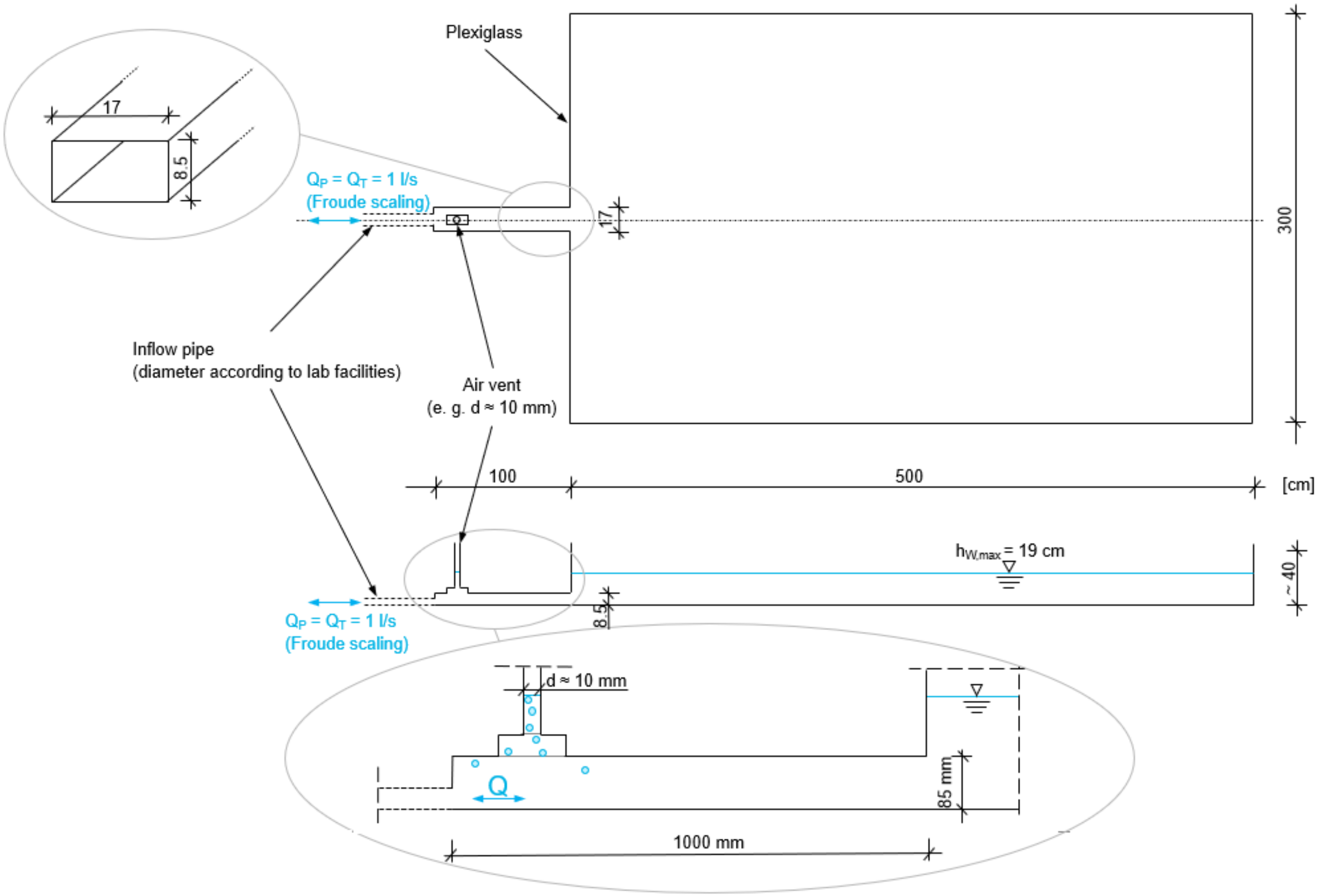


Appendix 11 - Sketch of the basin at scale M 1:175

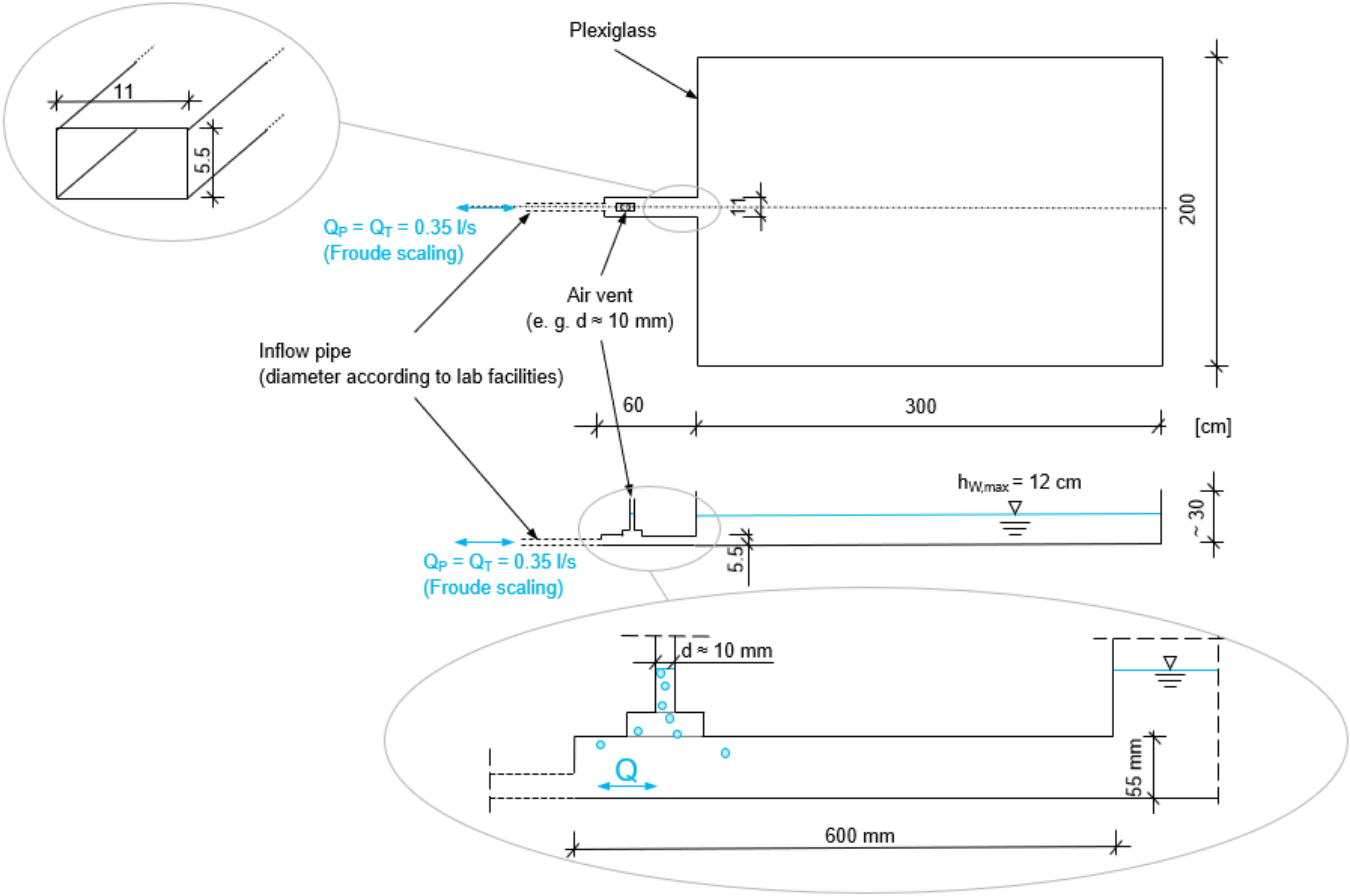


Appendix 12 - Sketch of the basin at scale M 1:275

## 1.5 Calculation of the turbulence limit

Calculation for the scale M 1:175:

$$Q = 405\ \frac{m^3}{s}$$

$$A = h * L_{tot.} = 15\ m * 30\ m = 450\ m^2$$

$$v = \frac{Q}{A} = \frac{405\ \frac{m^3}{s}}{450\ m^2} = 0{,}9\ \frac{m}{s}$$

$$d_h = \frac{4 * A}{U} = \frac{4 * h * L_{tot.}}{2 * h + 2 * L_{tot.}} = \frac{4 * 15\ m * 30\ m}{2 * 15\ m + 2 * 30\ m} = 20\ m$$

$$Re_P = \frac{v * d_h}{\nu} = \frac{0{,}9\ \frac{m}{s} * 20\ m}{1{,}002 * 10^{-6}\ \frac{m^2}{s}} = 17.964.071$$

$$Re_M = Re_P * M^{-1{,}5} = 17.964.071 * 175^{-1{,}5} = 7.760 > 2320$$

Calculation for the scale M 1:275:

$$Q = 401\ \frac{m^3}{s}$$

$$A = 450\ m^2\ (see\ above)$$

$$v = \frac{Q}{A} = \frac{401\ \frac{m^3}{s}}{450\ m^2} = 0{,}89\bar{1}\ \frac{m}{s}$$

$$d_h = 20\ m\ (see\ above)$$

$$Re_P = \frac{v * d_h}{\nu} = \frac{0{,}89\bar{1}\ \frac{m}{s} * 20\ m}{1{,}002 * 10^{-6}\ \frac{m^2}{s}} = 17.786.649$$

$$Re_M = Re_P * M^{-1{,}5} = 17.786.649 * 275^{-1{,}5} = 3.900 > 2320$$

## 1.6 Calculation of the flow change limit

Calculation for the scale M 1:175:

$$v_M = 0{,}07\ \frac{m}{s}; v_P = 0{,}9\ \frac{m}{s}$$

$$h_M = 0{,}03\ m;\ h_P = h_M * M^1 = 0{,}03 * 175^1 = 5{,}25\ m$$

$$Fr_M = \frac{v_M}{\sqrt{g * h_M}} = \frac{0{,}07}{\sqrt{9{,}81 * 0{,}03}} = 0{,}129 < 1$$

$$Fr_P = \frac{v_P}{\sqrt{g * h_P}} = \frac{0{,}9}{\sqrt{9{,}81 * 5{,}25}} = 0{,}125 < 1$$

Calculation for the scale M 1:275:

$$v_M = 0{,}053\ \frac{m}{s}; v_P = 0{,}89\bar{1}\ \frac{m}{s}$$

$$h_M = 0{,}03\ m;\ h_P = h_M * M^1 = 0{,}03 * 275^1 = 8{,}25\ m$$

$$Fr_M = \frac{v_M}{\sqrt{g * h_M}} = \frac{0{,}053}{\sqrt{9{,}81 * 0{,}03}} = 0{,}098 < 1$$

$$Fr_P = \frac{v_P}{\sqrt{g * h_P}} = \frac{0{,}89\bar{1}}{\sqrt{9{,}81 * 8{,}25}} = 0{,}099 < 1$$

## 1.7 Drawing of the final experimental setup

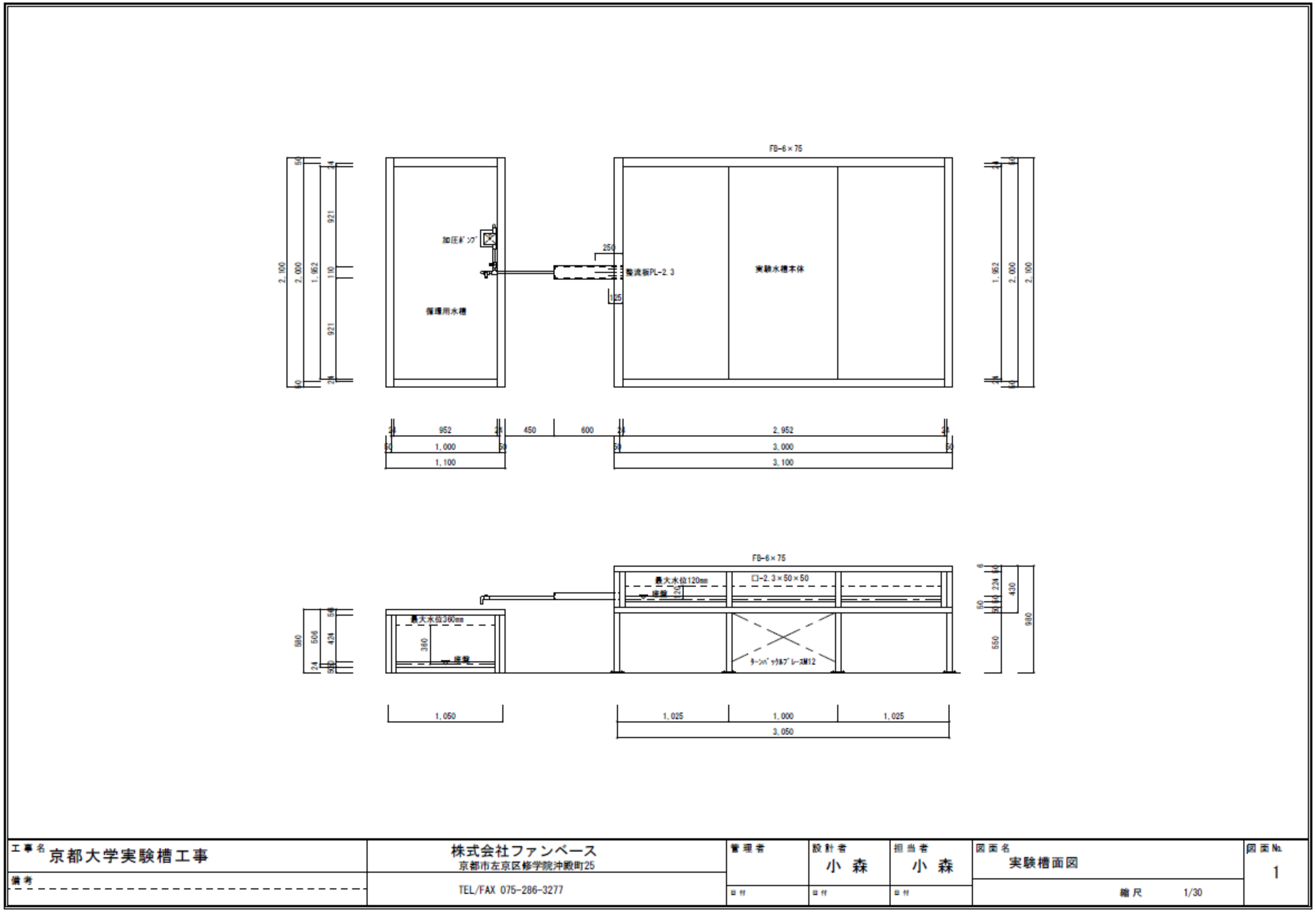


Appendix 13 - Technical drawing of the final experimental setup (Komori (小森) 2023)

## 1.8 Particle images

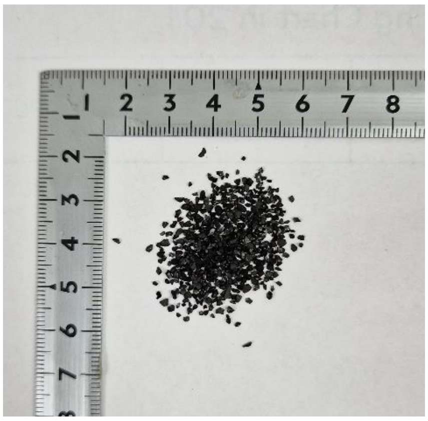
Appendix 16 - Charcoal coarse


Appendix 15 - Charcoal fine


Appendix 14 - Cork

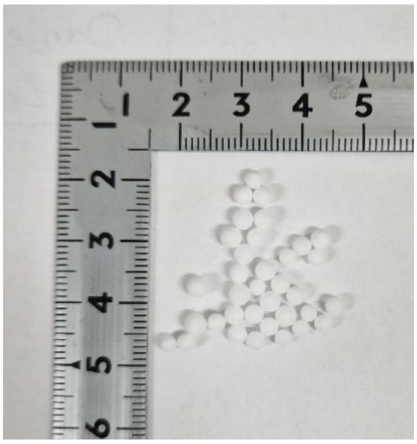
Appendix 18 – Polystyrene Beads

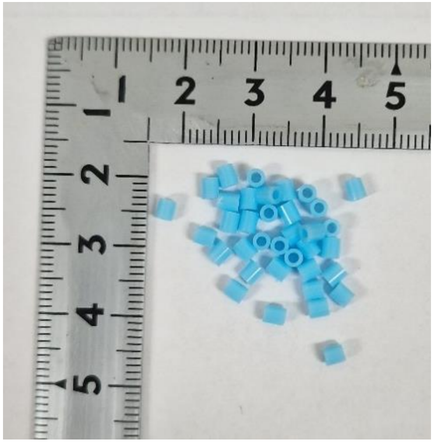
Appendix 17 - Polyethylene Beads


Appendix 19 – Crushed Walnutshells


Appendix 20 - Rice husk

## 1.9 Experiment instructions

**Experiment instructions - Upper basin of am pumped storage power plant**

Preparation steps:

1) Attach camera with suction cup holder to the ceiling directly above the center of the basin
   a. Connect to the "GoPro Quik" app on the cell phone for alignment of the frame and control of the camera
2) Clean the basin of any debris
3) Insert measuring tapes for orthorectification at both edges of the basin
4) Set the two spotlights at the edge of the basin, each with 2 lamps shining into the opposite corners of the basin to achieve even lighting

Inflow:

1) Fill the basin to a water depth of 2 cm
2) Stop the pump
3) Distribute seeding
4) Start the pump
5) Start video at a water depth of 3cm
   a. Track water level with legend on the edge of the basin for the video
6) Stop video after a water depth of 9 cm has been reached
7) Stop the pump
8) Close the inflow valve

Intermediate time: Predefined waiting time (4 minutes, 22 minutes, 40 minutes)

Drain:

1) Ensure that the seeding trap is attached to the drain
2) Open the drain valve
3) Start the video at a water depth of 9 cm
   a. Track water level with legend on the edge of the basin for the video
4) Stop video at 3 cm water depth

Follow-up:

1) Empty the basin

2) Clean the basin

3) Upload videos from camera to laptop / cloud

Remarks: Make sure the camera has sufficient storage space and battery life (one test requires about 55% battery and 50 minutes of storage space)

## 1.10 Recalculation of model limits

Turbulence limit:

$$Q = 329\ \frac{m^3}{s}$$

$$A = 450\ m^2\ (see\ above)$$

$$v = \frac{Q}{A} = \frac{329\ \frac{m^3}{s}}{450\ m^2} = 0{,}73\bar{1}\ \frac{m}{s}$$

$$d_h = 20\ m\ (see\ above)$$

$$Re_P = \frac{v * d_h}{\nu} = \frac{0{,}73\bar{1}\ \frac{m}{s} * 20\ m}{1{,}002 * 10^{-6}\ \frac{m^2}{s}} = 14.593.036$$

$$Re_M = Re_P * M^{-1{,}5} = 14.593.036 * 275^{-1{,}5} = 3.200 > 2320$$

Flow change limit:

$$v_M = 0{,}043\ \frac{m}{s};\ v_P = 0{,}73\bar{1}\ \frac{m}{s}$$

$$h_M = 0{,}03\ m;\ h_P = h_M * M^1 = 0{,}03 * 275^1 = 8{,}25\ m$$

$$Fr_M = \frac{v_M}{\sqrt{g * h_M}} = \frac{0{,}043}{\sqrt{9{,}81 * 0{,}03}} = 0{,}079 < 1$$

$$Fr_P = \frac{v_P}{\sqrt{g * h_P}} = \frac{0{,}73\bar{1}}{\sqrt{9{,}81 * 8{,}25}} = 0{,}081 < 1$$